

THE CENTRAL ENGINES OF NARROW-LINE SEYFERT 1 GALAXIES

C. J. RYAN AND M. M. DE ROBERTIS¹

Department of Physics and Astronomy, York University and
4700 Keele St., Toronto, Ontario, Canada M3J 1P3

S. VIRANI¹

Department of Astronomy, Yale University and
P.O. Box 208101, New Haven, CT 06520

A. LAOR

Physics Department, Technion and
Haifa 32000, Israel

AND P.C. DAWSON

Physics Department, Trent University and
1600 West Bank Drive, Peterborough, Ontario, Canada K9J 7B8

Draft version October 10, 2018

ABSTRACT

It has been suggested that Narrow-Line Seyfert 1 (NLS1) galaxies are evolutionarily young objects, powered by the accretion of gas onto central black holes that are significantly lower in mass than those found in typical broad-line Seyferts. We explore this hypothesis through the analysis of high-spatial resolution, near-IR imaging data obtained in J and K' for a sample of 11 NLS1s. Surface brightness profiles are separated into their constituent components using two-dimensional decomposition techniques. By employing the correlation between black-hole mass and host galaxy bulge luminosity, calibrated for near-IR wavelengths using 2MASS data, we determine the mean black-hole mass for our sample to be, in solar units, $\langle \log(M_{BH}) \rangle = 7.9$. Using the correlation between the size of the broad-line region and the monochromatic continuum luminosity, we obtain black-hole mass estimates under the assumption that the emission-line gas is in virial equilibrium. The mean black-hole mass derived from this relation is $\langle \log(M_{BH}) \rangle = 6.4$. It is found that the estimates obtained from the black-hole mass-bulge luminosity relation are systematically one full order of magnitude larger than those derived from the black-hole mass-broad-line region radius relation. We explore possible causes for this discrepancy in M_{BH} estimates and the ramifications for our understanding of the role played by NLS1s in AGN evolution.

Because numerical simulations constrain the start of the AGN duty cycle to a time shortly after a significant gravitational interaction, we examine the morphology and near-IR bulge colors of the NLS1 sample for evidence of recent encounters. The mean bulge color is found to be $\langle (J - K_s) \rangle = +1.85 \pm 0.58$, which is redder than that of both a matched sample of non-active galaxies and published estimates for broad-line Seyferts. The source of the unusual bulge colors may be an excess of flux, peaking at around $2.2 \mu\text{m}$, that has been detected near the centers of some NLS1s such as Mrk 1239. No evidence is found for light asymmetries or an extra stellar component that would indicate NLS1s are young objects. Finally, we postulate that there may be some interesting lines of circumstantial evidence suggesting that secular processes may be relevant in the evolution of NLS1s.

Subject headings: galaxies: Seyfert — galaxies: evolution — galaxies: photometry — infrared: galaxies — techniques: photometric

1. INTRODUCTION

The connection between the evolution of galaxies and that of the supermassive black holes that are known to lurk at their centers is a key issue in contemporary extra-

galactic studies. It is clear that Active Galactic Nuclei (AGN) represent an important, transient phase in the development of galaxies at all redshifts (Haehnelt & Rees 1993). The source of intense, non-thermal emission generated in the cores of AGN is widely accepted to be the accretion of material onto otherwise dormant black holes (Rees 1984; Peterson & Wandel 2000). However we may not yet fully appreciate the diversity of mechanisms that create the non-equilibrium conditions leading to accretion. Significant changes in gravitational potential can be produced by interactions between galaxies of comparable mass or by the consumption of dwarf satellite galaxies

Electronic address: cjryan@yorku.ca, mmdr@yorku.ca
Electronic address: svirani@astro.yale.edu
Electronic address: laor@physics.technion.ac.il
Electronic address: pdawson@trentu.ca

¹ Based on observations obtained at the Canada-France-Hawaii Telescope (CFHT) which is operated by the National Research Council of Canada, the Institut National des Sciences de l'Univers of the Centre National de la Recherche Scientifique of France, and the University of Hawaii.

(Osterbrock 1993). It also may be possible to trigger accretion through secular processes within the host galaxy such as bar-driven tidal instabilities, generating episodic bursts of nuclear activity (Kormendy & Kennicutt 2004).

An evolutionary link between black holes and their host galaxies is strongly suggested on the basis of correlations between the black-hole mass, M_{BH} , and various galaxy parameters. A good correlation has been found between M_{BH} and the central stellar velocity dispersion, σ_s , of the spheroid component of the host galaxy (e.g., Ferrarese & Merritt 2000; Gebhardt et al. 2000; Greene & Ho 2005a). The intrinsic scatter in this relation may be more significant at low black-hole masses, however (Bender et al. 2005). It has also been shown that M_{BH} is a constant fraction of the mass of the host spheroid (or, in the case of ellipticals, the total mass of the galaxy), with $M_{BH}/M_{sph} \simeq 0.0015$ (Magorrian et al. 1998; Marconi & Hunt 2003; Häring & Rix 2004). Under the assumption of a constant mass-to-light (M/L) ratio, this relation is frequently expressed in terms of the host bulge luminosity (e.g. Laor 2001; McLure & Dunlop 2001). While early studies found the scatter in this mass-luminosity relation to be substantial, recent progress in the amount and quality of available data has led to an improvement in the precision of the best-fit parameters (Marconi & Hunt 2003; Dong & De Robertis 2006). Marconi & Hunt (2003) also demonstrated the wavelength dependence of the scatter in the relation, with near-IR observations tracing the mass distribution better than optical data, generating a tighter correlation.

There is a general consensus in the literature that AGN exhibit these correlations independent of distance or luminosity, suggesting that they are a natural product of galaxy-black hole co-evolution (Kormendy & Richstone 1995; Barth, Greene, & Ho 2005). Yet there remains much debate as to how Narrow-Line Seyfert 1 galaxies, which constitute approximately 15% of the total low-redshift Seyfert population (Williams, Pogge, & Mathur 2002), fit into this picture. NLS1s are a subset of AGN exhibiting an overall spectral signature consistent with a Type 1 Seyfert, but with remarkably narrow permitted emission lines. More specifically, NLS1s are classified based on an observed broad component of H β emission with FWHM < 2000 km s⁻¹, strong Fe II emission, relatively weak [O III], and steeper soft x-ray continuum slopes than broad-line Seyfert 1s (Osterbrock & Pogge 1985; Boller, Brandt, & Fink 1996). Through a Principal Component analysis, Boroson & Green (1992) found that NLS1s dominate the extreme end of the ‘‘Eigenvector 1’’ anti-correlation between the Fe II and [O III] emission-line strengths. This relation is believed to be driven by the ratio of the luminosity of the source relative to its Eddington luminosity, L/L_{Edd} (Sulentic et al. 2000). Clearly, NLS1s occupy an important portion of AGN parameter space.

To account for the extreme properties of NLS1 galaxies, it has been conjectured that their central engines are black holes of relatively modest mass (typically of order $10^6 M_\odot$) (Boller, Brandt, & Fink 1996; Mathur 2000). This hypothesis can explain the narrow emission lines observed in these objects, under the assumption that the broad H β -emitting region is gravitationally dominated by the black hole. If the black holes in NLS1s are statistically smaller than in broad-line

Seyfert galaxies, elevated accretion rates would be required to account for the relatively normal observed luminosities (Pounds, Done, & Osborne 1995). Furthermore, it has been suggested that these objects represent an early stage in AGN evolution, during which the black-hole mass increases rapidly in a period of intense accretion (Mathur 2000). As the black hole grows in this scenario, the accretion rate gradually decreases and the NLS1 matures into a ‘‘normal’’ broad-line Seyfert (Grupe & Mathur 2004).

It remains unclear whether the aforementioned correlations with M_{BH} can be applied to NLS1s. Several authors suggest that NLS1s fall below the mass-luminosity correlation of other galaxies, resulting in smaller estimates of M_{BH} for a given bulge luminosity (Mathur, Kuraszkiewicz, & Czerny 2001; Wandel 2002). It has also been suggested that intense star formation activity could lead to overestimates of the bulge luminosity or, equivalently, underestimates of the (M/L) ratio (Nelson et al. 2004). The validity of the M_{BH} - σ_s correlation for NLS1s has also been questioned. It has been demonstrated by Barth, Greene, & Ho (2005) that AGN with small black holes follow the same relation as galaxies with more typical values for M_{BH} . Both Wang & Lu (2001) and Botte et al. (2004) estimate the velocity dispersion for NLS1 galaxy samples from measurements of [O III], and find that the M_{BH} - σ_s correlation is the same as for broad-line Seyferts. Conversely, a departure from the standard M_{BH} - σ_s relation for NLS1s was reported by Mathur, Kuraszkiewicz, & Czerny (2001), Grupe & Mathur (2004), and Bian & Zhao (2004). Each of these studies used [O III] as a surrogate for the velocity dispersion. It is interesting to note that different conclusions are reached in these studies even though the samples are similar.

A major thrust of this study is to compare black-hole masses derived from the well-known correlation between M_{BH} and the host galaxy luminosity for the NLS1 subset, hereafter the mass-luminosity correlation, with other mass estimates. To this end, we examine a sample of 11 NLS1s using high-spatial resolution, near-IR imaging data. The luminosities of the bulge components in J and K' are measured independently for each target. Black-hole masses are obtained by utilizing the mass-luminosity relation, calibrated to near-IR wavelengths. This work builds on previous studies by applying two-dimensional profile decomposition techniques to near-IR data of excellent quality, providing an accurate determination of the photometric properties of the host bulges. The results are compared to values of M_{BH} derived via the correlation between the radius of the broad-line region and the optical continuum luminosity, which has been calibrated using reverberation mapping mass estimates (Kaspi et al. 2000, 2005). This comparison is used to examine the role of NLS1s in the evolution of AGN.

In § 2 we outline the sample selection and describe the observations. The data reduction process, including the decomposition procedure, is included in § 3. The results and a discussion of their implications for the NLS1 paradigm are presented in § 4 and § 5, respectively. Conclusions are provided in § 6. Throughout this work, we adopt cosmological parameters of $\Omega_\Lambda = 0.7$, $\Omega_m = 0.3$ and a Hubble constant of $H_0 = 75 \text{ km s}^{-1} \text{ Mpc}^{-1}$.

2. OBSERVATIONS

To examine the possible role of NLS1 galaxies in the evolution of nuclear activity, a sample was selected from the Véron-Cetty & Véron (2001) catalog, Quasars and Active Galactic Nuclei, 10th Edition. Targets were chosen to be low-redshift ($z \leq 0.05$) and moderately bright (total $K' \leq +12.0$) in order to achieve the exceptional spatial resolution and signal-to-noise ratios necessary for accurate profile decompositions. Selecting targets from the Véron-Cetty & Véron catalog also ensured that a reasonable amount of complementary observations would be available, including optical spectroscopic data (Véron-Cetty, Véron, & Gonçalves 2001). A total of 150 objects are classified as NLS1s in the Véron-Cetty & Véron catalog. Of these, approximately 37 matching our selection criteria are visible in the Northern sky. We imaged 11 of these NLS1s in December 2002 through the broad-band J and K' filters at the 3.6-meter CFHT using KIR, the 1024×1024 HgCdTe array and near-IR camera, mounted at the f/20 output focus of the PUEO Adaptive Optics Bonnette (Rigaut et al. 1998). The focal plane scale of this system is $0.0348''/\text{pixel}$, providing a total field of view of $36'' \times 36''$. For all of the target observations, the galaxy nucleus was sufficiently bright to be used as the wavefront reference source. The photometric standard stars were also observed in the same way, acting as their own wavefront reference sources. This greatly facilitated the registration and co-addition of all dithered sequences, rendering other corrections unnecessary. Strehl ratios for the galaxy observations were estimated to be between 0.2 and 0.4, while for the standard stars the Strehl ratio was found to be approximately 0.5 (Beuzit & Hainaut 1998; Rigaut et al. 1998). A PSF FWHM of $0.2''$ was consistently measured from the standard star exposures, providing significant spatial over-sampling of the data. The key photometric properties of the galaxies, including morphological type, optical semi-major axis, and $K = +20$ mag arcsec $^{-2}$ isophotal radius, are provided in Table 1. We note that the K -band isophotal radii of the targets are between $6.4''$ and $26.1''$.

An exposure sequence for each object consisted of six spatially-dithered images, including two off-target exposures that were subsequently used to carefully monitor the near-IR sky and to provide accurate background subtraction. The data were acquired using the sequence T, T, B, T, T, B, with T representing an on-target exposure and B an off-target background exposure. The off-target exposures were dithered by between $1.6'$ and $2.3'$, depending on the size of the galaxy, to the East and West sides of the on-target field of view in order to avoid contamination by the extended disks of the galaxies. This procedure ensured that the on-target images were bracketed, both spatially and temporally, by the background frames. The on-target exposures were typically dithered by approximately $16''$ in a four-point box pattern that placed the galaxy nucleus in each of the detector's quadrants. Total on-target exposure times varied between 80 and 1920 seconds, chosen to maximize the signal while ensuring that the detector response remained linear. Equal exposure times were used for all images in each sequence. The mean airmass for each data set was typically between 1.0 and 1.2. A summary

of the observation log is provided in Table 2.

3. DATA REDUCTION

The data were reduced using standard IRAF procedures, including the construction and application of bad pixel masks, the removal of dark current, and a flat-field correction (including any large-scale gradients). A crucial step in the reduction and analysis of near-IR images is the accurate subtraction of the sky background. The characterization of the background level and pattern is particularly challenging, as it has been shown that the mean level at the CFHT site can vary by 0.7% and 0.5% in J and K' , respectively, on time scales of one minute (Vaduvescu & McCall 2004). Failure to take this into consideration could potentially lead to photometric errors when imaging extended sources with lengthy integration times. Because of the relatively large angular size of the targets compared with the detector's field of view, it was impractical to determine the background level using adjacent on-target exposures. Instead, accurate background subtraction was achieved by carefully monitoring the two off-target exposures from each data set. An inspection of the median and mode for each pair of off-target frames indicated that the background level and underlying patterns were constant to within 1%, allowing us to use the combined off-target frames for background subtraction.

We then examined the on-target exposures, both before and after background subtraction, to search for any systematic uncertainties introduced by this procedure. As the on-target dither pattern situated the galaxy nucleus sequentially in each of the detector's four quadrants, we monitored the image statistics of the opposite quadrant carefully. Variations in the median count rate among the image corners were always within underlying statistical uncertainties. The residual flux levels of the corners of the background-subtracted images were consistently near zero, with no residual gradients present. This gave us confidence that the background had been successfully and appropriately removed in all target exposures.

The dithered on-target exposures were combined into $56'' \times 56''$ mosaic images using the IRAF package *irred.irmosaic*. For three galaxies, multiple image sets were obtained in K' , allowing independent mosaics to be generated. This served as a useful check on the consistency of the data reduction and analysis processes.

3.1. Bulge-Disk Decomposition

The surface brightness profiles of the reduced mosaic images were then examined to determine the relative flux associated with the bulge component. To accomplish this, the two-dimensional profile fitting algorithm GALFIT v2.0 was employed. GALFIT allows the user to model the light profile of a target using a suite of analytic functions, including Gaussian, exponential, Sérsic/de Vaucouleurs, and Nuker profiles. The optimal fit is determined, based on the user's selection of input parameters, by minimizing the χ^2 residual between original and model profiles. Details of the minimization routine are provided in Peng et al. (2002).

While GALFIT is capable of fitting a PSF-convolved Gaussian to account for a point source, in the interest of limiting the number of free parameters in the model and

to best ensure the parameters are physically realistic, an alternative method was used to subtract the contribution of the active nucleus to the integrated flux. This *shift-scale-subtract* (sss) routine involves using a high signal-to-noise ratio, isolated point source such as a photometric standard star observed under similar conditions to model the AGN (Virani, De Robertis, & VanDalsen 2000). For each target, a standard star observed close in time was selected as a template point source. The stars were imaged with the AOB activated, using the same dither pattern as employed for the target observations. The spatial and temporal stability of the standard stars was monitored by examining the reduced exposures. It was found that the stellar PSFs were consistent to within 0.02 magnitudes, and the FWHM varied by less than 0.05". To subtract the nuclear component, the star was aligned to the center of the galaxy as estimated from elliptical isophote fitting via the *ellipse* package. Accuracies of ± 0.1 pixel are achievable for the spatial alignment by monitoring asymmetries in the light profile of the difference image. The scaling of the nuclear PSF was judged to be that which produced a nearly flat profile in the central 0.4". The average contribution of the nuclei to the total galaxy flux was determined to be approximately 15% in J and 9% in K' . It was thus possible to assess the nuclear contribution to better than 1% of the total galaxy luminosity. Appropriate nuclear scale factors were determined independently for the J - and K' -band images.

The nucleus-subtracted galaxy images were then modeled as the sum of a bulge and, when necessary, disk component using GALFIT. Galaxy disks were fit using an exponential profile (Freeman 1970). The analytic form of galaxy bulges is less clear, and has been discussed extensively in the literature. Most early studies represented bulge light as a de Vaucouleurs (1948) $r^{1/4}$ profile, similar to that used for elliptical galaxies. However, for many galaxies the profile fails to accurately reproduce the shape of the bulge at all radii (Caon, Capaccioli, & D'Onofrio 1993). This departure from the $r^{1/4}$ profile is of greatest concern for early-type galaxies, where a significant fraction of the total galaxy light comes from the bulge component. It has been demonstrated that bulges are better described using the more general Sérsic (1968) $r^{1/n}$ profile (Andredakis, Peletier, & Balcells 1995), which reduces to a de Vaucouleurs profile for $n = 4$. Sérsic profiles were applied to model the bulge light for the NLS1 sample with the index, n , a free parameter to be determined by GALFIT. As all of the targets are early-type galaxies, no additional components were required to account for features such as spiral arms.

Initial estimates for the disk scale radii were taken from the 2MASS Extended Source Catalog (XSC), recalibrated to the KIR image scale. The XSC images have a relatively coarse $1''/\text{pixel}$ focal plane scale and an integration time of 7.8 seconds. As such, the published scale parameters for these moderately faint objects, which have a mean 2MASS $K_s = +10.8$, were treated as initial estimates to be determined more accurately by GALFIT.

Starting values for the bulge scale radii were then estimated from an examination of disk-subtracted, one-

dimensional surface brightness profiles. The position angle, ellipticity and a_4 "diskiness parameter" were also estimated from elliptical isophote fitting to the nucleus-subtracted images. For the Sérsic index, an initial estimate of $n = 4$ was used, as the targets are generally early-type galaxies and it has been demonstrated that there is a trend of decreasing index as morphological type proceeds from early to late (Graham 2001). All of these parameters were allowed to vary within the χ^2 minimization process, however. The luminosity bulge-to-disk ratio was estimated from the empirical relation with Hubble stage originally presented in Simien & de Vaucouleurs (1986) and derived from K -band data in Graham (2001).

For each target, we used GALFIT to first obtain one-component fits to the disks of the galaxies. Pixel masks aligned to the isophotal centers of the galaxies were used to block the bulge components in these initial model fits. The results were then used as estimates of the input parameters in two-component fits, again allowing all parameters to vary in order to find the global χ^2 minimum. For these fits, we did not apply pixel masks to any sections of the mosaic images and fit the galaxy profiles to $r = 0$.

It is also necessary that the relevant parameters be physically realistic. For three targets, Mrk 359, Mrk 1044 and MCG08.15.009, it was necessary to constrain one of the free parameters in order to avoid convergence to a non-physical analytic fit. For these galaxies, the bulge scale radius was held fixed to the value provided by the 2MASS XSC. Residual images were also visually examined for any significant features or asymmetries.

Proper background subtraction is essential to measure accurate integrated fluxes for each component of the galaxy. To estimate the uncertainties in the fitted parameters to reasonable uncertainties in the background level, we performed fits to the data with sky levels set systematically high and low by one standard deviation in the background. The same input parameters used to derive the optimal fits were employed in these tests. This technique is similar to that applied to one-dimensional decompositions by Graham (2001). In some cases, negative fluxes introduced by background over-subtraction prevented GALFIT from converging on a meaningful solution. Based on the results of these extensive tests, however, it was established that conservative uncertainties in the bulge fits resulting from imperfect background subtraction are less than 0.1 magnitudes.

Separate model fits to the J and K' images were obtained for each galaxy. Plots of the J -band surface brightness decompositions are shown in Figures 1 through 11. For each target, the relative contribution of the components are presented in log space; residuals to the fit are plotted separately in linear space. For the K' -band decompositions, we find that there is a consistent pattern in many of the residual profiles on angular scales less than $1''$ from the galaxy center, such that a broad negative peak is followed by a small upturn. This is illustrated in Figure 12, which presents the K' -band profile for Mrk 1126. It is conceivable that the pattern, which has an insignificant effect on total bulge magnitudes, may be due to limitations in our nucleus-subtraction routine. In order to search for any systematic effects introduced by the sss-technique, we performed profile decompositions on images in which the point sources were purposely over-

subtracted and under-subtracted by 10%. This level of uncertainty is greater than could reasonably be expected from a careful subtraction of the nucleus. We found in these cases that the bulge magnitudes varied by of order ± 0.03 magnitudes. The reason this has no significance on total bulge magnitudes is essentially because the angular extent of the model bulge profiles are between $2''$ and $8''$. Since nuclei affect only the central $0.2''$, their influence is limited to a fraction of the inner 1% of the two-dimensional bulge profiles.

In employing the sss-technique, it is assumed that the PSFs associated with the active nuclei can be adequately modeled as scaled versions of the photometric standard stars. However, small discrepancies could arise from effects such as changes in the airmass of the observations or contamination from the AGN host galaxies. Furthermore, differences in the wavefront reference source magnitudes between the AGN and standard star observations resulted in small variations in the Strehl ratios. This could produce slight differences in the AO-corrected PSFs. To further verify that the subtraction of the flux associated with the active nucleus did not introduce any systematic effects on the bulge fits, we performed three-component fits to the data using GALFIT. In addition to the bulge and disk components, a nuclear point source was included, represented by a Gaussian function. The bulge magnitudes and Sérsic indices derived from these fits were consistent with the results obtained using the sss-technique. The quality of the fits, as parameterized by the reduced χ^2 values, were also comparable. Additionally, two-component (bulge+disk) fits were performed on the non-PSF-subtracted images. The output bulge magnitudes were again similar to the results presented in Table 3, albeit with slightly higher Sérsic indices and increased residuals. These results are not surprising, given that the flux associated with the nucleus is of order a few percent of the total galaxy flux, and is confined to the central 1% of the model fits. From these tests it was concluded that the sss-technique is robust, and does not compromise the model bulge parameters.

The small but systematic K' -band residuals may also reflect a departure of the analytical model from the physical structure near the center of the bulge component that is resolved by our data. An additional source of emission may influence the surface brightness on scales less than $1''$ from the nucleus (Rodríguez-Ardila & Mazzalay 2006). This option is discussed in greater detail in § 5. The net effect of these small, systematic residuals on the total integrated luminosities of the galaxy components is negligible.

For the three galaxies that were observed twice in K' , independent fits provided a useful check of the consistency of the fitting procedure. We found that the bulge magnitudes obtained from these images were consistent within the formal uncertainties. Absolute bulge magnitudes were then calculated using redshift information taken from the literature and Galactic extinction corrections based on the dust maps presented in Schlegel, Finkbeiner, & Davis (1998). The results are summarized in Table 3.

4. BLACK-HOLE MASSES

Black-hole mass estimates for AGN are frequently obtained by employing the relation between the size of the

broad-line region and the monochromatic continuum luminosity at 5100 \AA , the mass-radius relation. We will compare these results with masses derived from the well known correlation between M_{BH} and the host bulge luminosity, the mass-luminosity relation, using the results obtained from the two-dimensional profile decompositions. In the following subsections we discuss these techniques in greater detail, and present the resulting black-hole mass estimates.

4.1. The Mass-Radius Relation

Reverberation mapping is widely considered to be a reliable method to obtain accurate M_{BH} estimates in Seyfert 1 galaxies, for which direct probing of the black-hole sphere of influence is not possible due to the intense nuclear emission. Correlations with host galaxy parameters derived from reverberation mapping results are generally consistent with those of non-active galaxies with secure values of M_{BH} (Ferrarese & Ford 2005). However direct measurements of the time delay between fluctuations in continuum and line emission can be challenging and require long-term monitoring of the source. As a consequence, estimates of M_{BH} are more commonly generated using secondary, indirect methods such as exploiting the correlation between the radius of the broad-line region and the monochromatic continuum luminosity at optical wavelengths (Kaspi et al. 2005):

$$\frac{R_{BLR}}{10 \text{ lt} - \text{days}} = (2.23 \pm 0.21) \left[\frac{\lambda L_{\lambda}(5100 \text{ \AA})}{10^{44} \text{ erg s}^{-1}} \right]^{0.69 \pm 0.05}. \quad (1)$$

Based on a sample of six objects with $\text{FWHM}(\text{H}\beta) < 2000 \text{ km s}^{-1}$, Peterson et al. (2000) suggested that this relation can be extended to the NLS1 subset. This conclusion is supported by the observation that the continuum luminosity at 5100 \AA is comparable in NLS1s and broad-line Seyferts (Grupe et al. 2004). However, the low optical variability that is characteristic of NLS1s makes secure reverberation mapping masses of these objects particularly difficult to obtain, as demonstrated by the small number that have been successfully monitored (e.g. Shemmer et al. 2001).

Optical spectra were published by Véron-Cetty, Véron, & Gonçalves (2001) for a large number of NLS1s, including seven of the objects in our sample. The data were obtained with the CARELEC spectrograph mounted to the 1.93-meter telescope at the Observatoire de Haute-Provence, providing a resolution of 200 km s^{-1} at $\text{H}\beta$. The contribution of Fe II emission was removed using a template spectrum generated from observations of the NLS1 I Zw 1, according to the procedure discussed in Boroson & Green (1992). The published spectra have a wavelength range of 4750 to 5100 \AA . The paper also includes values for the FWHM of the broad component of $\text{H}\beta$ for each object, taken from the literature. We measured the monochromatic continuum luminosity at 5100 \AA from these spectra, correcting for Galactic extinction. The results were used to estimate the radius of the broad-line region according to (1). Assuming the emission-line gas is in virial equilibrium with the central black hole, estimates of M_{BH} for each object may then be obtained using the following expression:

$$M_{BH} = R_{BLR} G^{-1} (k v_{\text{H}\beta})^2. \quad (2)$$

The constant k is a function of the geometry of the broad-line region. Assuming the line-emitting gas is distributed purely isotropically, as Kaspi et al. (2000) and Wandel (2002), $k = \sqrt{3}/2$.

For each of our targets with spectroscopic data available in Véron-Cetty, Véron, & Gonçalves (2001), values for the continuum luminosity at 5100 Å, the FWHM of the broad component of H β , and the calculated black-hole masses are included in Table 5. The mean value of M_{BH} for the seven NLS1s is $\langle \log(M_{BH}) \rangle = 6.3$, in agreement with the idea that black holes in NLS1s are statistically less massive than broad-line Seyferts. The assumption of a spherically symmetric gas distribution, however, is likely to be an oversimplification. A physically more meaningful model may include a gas disk in addition to an isotropic component (McLure & Dunlop 2001). The introduction of a disk component in the broad-line region would increase the virial mass estimates presented here by a factor of three.

Greene & Ho (2005b) propose a correlation between the radius of the broad-line region and Balmer emission-line luminosities. Using a sample of 229 objects taken from the Sloan Digital Sky Survey (York et al. 2000), they obtain an empirical relation between M_{BH} and the H β line luminosity of the form:

$$M_{BH} = (3.6 \pm 0.2) \times 10^6 \left[\frac{L_{H\beta}}{10^{42} \text{ erg s}^{-1}} \right]^{0.56 \pm 0.02} \left[\frac{\text{FWHM}_{H\beta}}{10^3 \text{ km s}^{-1}} \right]^2 \quad (3)$$

In formulating this relation, the authors derive the mass-luminosity relation independent of Kaspi et al. (2005). This provides a second method to estimate masses based on reverberation mapping.

We measured the H β line flux for the seven NLS1s from our sample with available optical spectra and used the results to compute the black-hole mass in each object according to (3). The values obtained for L(H β) and the resulting estimates of M_{BH} are included in Table 5. The average unweighted black-hole mass was found to be $\langle \log(M_{BH}) \rangle = 6.4$, again consistent with the notion that black holes in NLS1s are statistically less massive than those found in broad-line Seyferts.

4.2. The Mass-Luminosity Relation

As discussed in § 1, it is generally accepted that the slope of the correlation between M_{BH} and host bulge luminosity is consistent for both non-active galaxies and “typical” Seyfert galaxies. However, it remains a matter of debate as to whether the relation can be extended in the same form to the NLS1 subset. Using the results obtained from our profile decompositions, we now derive estimates of M_{BH} under the assumption that the slope of the correlation is the same for all Seyfert galaxies, including NLS1s. We then compare these mass estimates to those obtained in § 4.1. The results are presented in this manner in order to avoid *a priori* assumptions about the accuracy of the black-hole masses obtained from the mass-radius relation. While reverberation mapping masses are generally secure, only a handful objects that could be classified as NLS1s have been directly observed using this technique. It is conceivable that other factors such as the orientation of the broad-line region could affect the observed line widths, potentially leading

to underestimates of the black-hole masses. Such issues do not affect the mass-bulge luminosity relation.

The correlation between M_{BH} and the mass of the spheroid component of the host galaxy is frequently quantified in terms of the B -band magnitude (e.g. Ferrarese & Ford 2005). However, the blue luminosity is biased by the presence of young, hot stars and does not necessarily best represent the underlying mass distribution. Near-IR wavelengths are less sensitive to this bias, and are less affected by dust extinction. This is evident from a comparison of the mean extinction curves in B and K' . Using values presented in Mathis (1990), the ratio of B - to K' -band optical depths is approximately 12.3. Based on the extinction values for our target fields, we estimate that the attenuation of light in B due to the presence of Galactic dust is more than 11 times greater than that in K' . Hence the scatter in the correlation can be reduced by employing near-IR data, as first demonstrated by Marconi & Hunt (2003).

We calibrated the mass-luminosity relation for near-IR passbands using a sample of 16 bright elliptical galaxies with secure mass estimates obtained by resolving the black-hole sphere of influence as reported by Ferrarese & Ford (2005). The assumption that ellipticals are kinematically similar to the bulge components of spiral galaxies and therefore follow the same correlation is supported by observational evidence for consistent Fundamental Plane relationships (Kormendy & Illingworth 1982; Falcón-Barroso, Peletier, & Balcells 2002). Excluding spiral galaxies from the sample eliminates the need for separating the total integrated flux into bulge and disk components, thus minimizing the scatter in the correlation. Furthermore, we reject several ellipticals with secure M_{BH} estimates for the following reasons. Cygnus A is known to be a member of a rich cluster of galaxies, and thus may be influenced by a complex gravitational potential. Two other galaxies, NGC 821 and NGC 2778, have estimated spheres of influence that are smaller than the spatial resolution of the data. For each remaining object, the total magnitude in the 2MASS near-IR bandpasses of J and K_s were extracted from the XSC. It is important to note that the response curves of the 2MASS filter set are not identical to those of the CFHT filters used for our NLS1 observations. The necessary photometric transformations are now discussed.

Absolute magnitudes were calculated for all but two of the galaxies using distance estimates from Tonry et al. (2001). As data were not available in Tonry et al. for NGC 6251 and NGC 7052, we determined luminosity distances using redshifts obtained from the Third Reference Catalog of Bright Galaxies (RC3)(de Vaucouleurs et al. 1991). A summary of the properties of the galaxies used to calibrate the mass-luminosity relation is presented in Table 4.

In Figures 13 and 14, we plot the logarithm of M_{BH} , in solar masses, versus the absolute magnitude in J and K_s for the sample of elliptical galaxies. The best-fit slopes to the data were determined from a linear least-squares fit, weighting the parameters by their uncertainties (Press et al. 1992). The mass-luminosity correlations in J and K_s have the following forms:

$$\log M_{BH} = (-0.43 \pm 0.04)(M_J + 22.52) + (8.17 \pm 0.09) \quad (4)$$

$$\log M_{BH} = (-0.44 \pm 0.04)(M_{K_s} + 23.45) + (8.17 \pm 0.09). \quad (5)$$

Our results are consistent within uncertainties with both the K_s -band fit presented in Dong & De Robertis (2006), obtained using the same sample criteria, and the results of Marconi & Hunt (2003), whose sample includes spiral galaxies.

In order to use these correlations, it was necessary to convert the bulge magnitudes obtained by GALFIT from the Mauna Kea Observatories (MKO) photometric system to the 2MASS system. Color transformations for various filter sets are available through the 2MASS website². The transformations for the MKO system are:

$$K_{s,2MASS} = K_{MKO} + (0.002 \pm 0.004) + (0.026 \pm 0.006)(J-K)_{MKO} \quad (6)$$

$$(J-K_s)_{2MASS} = (1.037 \pm 0.009)(J-K)_{MKO} + (-0.001 \pm 0.006). \quad (7)$$

However, these transformations are valid for the K filter and not K' . Wainscoat & Cowie (1992) compare the K' filter to K , and suggest a color transformation of the form

$$K' - K = (0.22 \pm 0.03)(H - K). \quad (8)$$

In the absence of H -band data for our sample galaxies, we adopted a mean $(H-K)$ color estimated from Fioc & Rocca-Volmerange (1999). Using a sample of approximately 1000 galaxies, the authors computed near-IR colors as a function of host morphology. They determine a median $(H-K)$ for ellipticals of approximately 0.20 ± 0.01 , rising to 0.27 ± 0.01 for spirals. Assuming that the bulge colors for our galaxies are similar to that of ellipticals, a conversion from K' to K is possible. Combining this result with the color transformation between K and K_s , it can be seen that magnitudes measured in K' and K_s are the same within photometric errors. This is supported by an inspection of the transmission functions for K' and K_s filter, which are very similar (Kim et al. 2005). A non-trivial transformation between J_{MKO} and J_{2MASS} is required of course.

It was also necessary to adjust our bulge magnitudes by applying modest K -corrections to our data. Corrections were taken from Poggianti (1997) who used evolutionary synthesis models based on redshift and as a function of host morphology. When necessary, corrections were estimated from a linear interpolation between redshift bins of width 0.02. The measured bulge magnitudes were then inserted into (4) and (5) to estimate M_{BH} for each NLS1 target. The results are presented in Table 5. The unweighted mean mass was found to be $\langle \log(M_{BH}) \rangle = 7.9$.

As a consistency check, we applied the Simien & de Vaucouleurs (1986) relationship between the luminosity bulge-to-disk ratio and Hubble stage. This method is less reliable than our more accurate component decomposition due to the large dispersion in the relation. Using a sample of 118 spiral galaxies, representing morphological stages S0/a through Sc, Dong & De Robertis (2006) have calibrated the relation for the 2MASS K_s -band. The relation is represented by the following cubic equation:

$$\Delta m_{K'} = 0.297(T+5) - 0.04(T+5)^2 + 0.0035(T+5)^3. \quad (9)$$

Of the 11 NLS1s included in our sample, published morphological classes were available for seven galaxies. Preliminary classifications were made for two additional galaxies, MCG 08.15.009 ($T=-1$) and PG 1016+336 ($T=1$), based on a visual inspection of our high-spatial resolution data. Morphological information was not available for Mrk 734 and IRAS 04596-2257. Applying (9) to the sample, bulge magnitudes were calculated and compared to those derived by GALFIT. The results are included in Table 5. While the scatter in the measurements for individual galaxies is substantial, the mean bulge magnitudes are consistent to within 0.02 magnitudes, further establishing that the values generated by GALFIT do not suffer from any systematic errors.

5. DISCUSSION

The black-hole masses presented in the previous section are plotted as a histogram in Figure 15. There is a clear offset between values obtained using different correlations. We find that the estimates of M_{BH} calculated from the near-IR bulge luminosities are, on average, more than one order of magnitude larger than those obtained from the mass-radius relation. The measurement uncertainty for each object is typically 0.25 dex, which is insufficient to account for the difference in the results. Therefore, one (or more) of the assumptions made in formulating the correlations must not be applicable to this particular subset of active galaxies. In the following subsections, we consider the evidence supporting the extension of each correlation to NLS1s, and discuss the impact of these results on our understanding of these objects.

5.1. Are Black Holes Less Massive In NLS1s?

The most common interpretation of the observed spectral characteristics of NLS1s is that the central black holes are less massive than those found in broad-line Seyfert galaxies. This hypothesis is supported in the literature by studies that employ the mass-radius correlation as calibrated by reverberation mapping studies (e.g. Grupe & Mathur 2004). Indeed, we find that for our sample the mean value of M_{BH} determined from (1) and (2) is $\langle \log(M_{BH}) \rangle = 6.4$. If we accept the virial mass estimates obtained from the mass-radius relation, the results from our profile decompositions provide evidence that the galaxy bulges in our sample are more luminous than predicted by the mass-luminosity relation. This is illustrated in Figures 13 and 14, in which we compare the NLS1 black-hole masses as determined from the mass-luminosity relation and the mass-radius relation. The estimates of M_{BH} derived from the mass-radius relation lie well below the best-fit line calculated from ellipticals with secure M_{BH} estimates.

It has been proposed that the departure of NLS1s from the mass-luminosity relation is the result of the contribution of excess flux from either bursts of nuclear star formation or AGN emission (Nelson et al. 2004). We exercised great care in subtracting the nuclear component from our high-resolution imaging data, however. Any residual emission inadvertently included in measuring the bulge magnitude would be negligible, and certainly would not alter the subsequent estimates of M_{BH} by one full order of magnitude. Rather, any errors in the nuclear subtraction routine would likely involve an over-

² http://www.ipac.caltech.edu/2mass/releases/allsky/doc/sec6_4b.html

correction, leading to underestimates of the black-hole masses. The estimated bulge scale radii are typically larger than $0.5''$, and all are greater than the nominal PSF FWHM of $0.2''$. Therefore, we are confident that the derived parameters, including the bulge magnitudes, are both physically reasonable and accurate.

If black holes are less massive in NLS1s, there must be a physical explanation for the breakdown of the mass-luminosity relation. One interpretation is that there is an inherent time delay between an increase in the mass of the bulge through star formation and the growth of the central black hole due to accretion. In this scenario, sufficient time passes after a gravitational interaction between galaxies for the bulge to virialize and stars to form before gas inflow triggers significant nuclear activity. One could imagine that accretion onto the central black hole is then halted by feedback mechanisms as the mass becomes consistent with that of a “normal” Seyfert galaxy. Numerical simulations of interactions by Di Matteo, Springel, & Hernquist (2005) suggest that such galactic nuclei undergo a period of rapid accretion towards the end of a merger event due to the elevated gas content near the core. It is during this phase that the central black holes can increase in mass by a significant fraction, and the target emerges as an AGN. During this period of rapid growth, the accretion rate can approach the Eddington limit. If NLS1s are indeed evolutionarily young objects at the start of the AGN duty cycle, these simulations constrain the NLS1 phase to a time relatively soon after a gravitational interaction, a time when one might expect significant morphological asymmetries in the host galaxies and particularly the centers.

In order to search for such morphological evidence, we divided the reduced K' -band mosaics by the associated J -band images. We then applied an unsharp mask by convolving the quotient image with a Gaussian function with a standard deviation of $1.5''$. No evidence was found of light asymmetries or tidal features that would be indicative of a late-stage merger. Furthermore, we note that spectroscopic detections of Seyfert nuclei in systems currently undergoing a strong interaction (e.g. Liu & Kennicutt 1995; Vanzi, Alonso-Herrero, & Rieke 1998) are difficult to explain if bulge growth and AGN fueling are temporally well separated.

To further investigate the claim that NLS1s are evolutionarily young, we compared the near-IR bulge colors of the objects in our study to a subset of non-active, early-type galaxies taken from the sample examined by Dong & De Robertis (2006). Three non-active galaxies were selected for each NLS1, matched according to morphological class and absolute magnitude of the total galaxy. Of the 27 objects selected, we note that nine are actually identified as containing a LINER nucleus. The mean bulge color for this subset of galaxies is equivalent to the mean for the other galaxies in our non-active sample. Therefore, their inclusion does not adversely affect our results. Using 2MASS XSC imaging data, the $(J-K_s)$ colors of the bulge components of the non-active objects were computed with GALFIT. The galaxy parameters derived from the fits, including bulge magnitudes, are presented in Table 6. The bulge $(J-K_s)$ colors for the non-active galaxies and NLS1s are plotted against the absolute bulge magnitudes in K_s in Figure 16. The mean bulge color for the non-active sample is $(J-K_s) = +1.10$

± 0.04 , while for the NLS1 sample, the mean color was found to be $(J-K_s) = +1.85 \pm 0.58$.

In the absence of two-dimensional profile decompositions for a matching sample of broad-line Seyferts, we compare our NLS1 colors to results culled from the literature. Hunt et al. (1997) measured the near-IR colors of galaxies hosting Seyfert and starburst nuclei. The mean color of the inner 3 kpc of the Seyfert 1 galaxies in their sample was found to be $(J-K) \simeq +1$. However, the inner $4''$ were masked to exclude contamination from the active nucleus; hence the measured colors more accurately represent the inner disk component rather than the bulge. Their use of an early-generation InSb 62x58 IR array also limits the comparison to our high-spatial resolution, AO-corrected data.

A comparison of the near-IR colors of Seyfert and non-active spiral galaxies is presented in Márquez et al. (2000). Using 1-dimensional profile decompositions, the authors conclude that the bulge and disk components of the two galaxy samples are similar in terms of their mean $(J-K)$ color and Fundamental Plane relation. However there is significant scatter in the measured bulge colors of the 18 AGN in their sample, and while the mean bulge color was determined to be $(J-K) = +1.25$, several galaxies have a bulge color in excess of $+1.5$. One object in particular, NGC 4253, was found to have an exceptionally red bulge, with $(J-K) = +4.4$. Interestingly, while this galaxy is classified as a Seyfert 2 in Márquez et al. (2000), it is identified as a NLS1 in Crenshaw, Kraemer & Gabel (2003).

We find that of the 11 NLS1s in our sample, four have a bulge color of $(J-K_s) \simeq +1$ to $+1.5$, consistent with the sample of non-active galaxies and other studies of broad-line Seyfert galaxies. However, six of the targets have a bulge color of $(J-K_s) \simeq +1.9$, and for one, Mrk 1239, we measure $(J-K_s) = +3.0$. We find no evidence for systematic effects that would lead to errors in our measured colors; on the contrary, the targets with the reddest bulge colors are also the model fits with the lowest residuals, as parameterized by the reduced χ^2 values.

The near-IR spectrum of Mrk 1239 may provide a clue to the source of the unusual bulge colors. A significant bump in nuclear continuum emission, centered on $2.2 \mu\text{m}$, was detected by Rodríguez-Ardila & Mazzalay (2006). Given the resolution limit of approximately $1''$ for their data, the authors constrain the source of this emission to the central 380 pc, which is well outside the seeing disk of our imaging data. A similar flux excess has been detected in the NLS1s Mrk 766 (Rodríguez-Ardila, Contini, & Viegas 2005) and I Zw 1 (Rudy et al. 2000). Comparing the spectrum of Mrk 1239 to that of the NLS1 Ark 564, they find the latter does not exhibit any excess continuum emission in the K -band. Hence the feature appears to be present in some, but curiously not all, NLS1 galaxies. This may explain the large scatter in the $(J-K_s)$ bulge colors of our sample.

Because the observed K_s -band excess is constrained to the central regions of the targets, we closely examined the inner bulge colors of our targets. We find that some of the NLS1s in our sample exhibit a gradient, such that the bulge colors become redder with decreasing radius. This is consistent with the view that an additional source

of flux is detected at $2.2 \mu\text{m}$ in the inner regions of some of our NLS1 targets. Consequently, our K_s -band bulge profiles may be influenced by this component, producing the small but systematic residual pattern evident in Figure 12. Fitting the peak with a blackbody temperature of 1200 K, Rodríguez-Ardila & Mazzalay (2006) suggest that the source of the excess flux is hot graphite dust emission near the active nucleus. This explanation, however, cannot account for the spatial extent of the emission as demonstrated by the observed color gradients.

We also note that the estimates of M_{BH} derived from the profiles in K_s are generally larger than those obtained from the J -band fits. Given the possible presence of an additional source of flux near the centers of some NLS1s, we consider the mass estimates in J to be more robust, and caution against the use of K_s -band data to measure NLS1 host bulge luminosities.

In summary, while we cannot formally exclude the low-mass interpretation, we find no evidence from our data that NLS1s as a group have morphological asymmetries or extra stellar components distinct from normal Seyfert galaxies that would suggest that these objects contain a recently formed AGN. It may well be that there is a modest flux excess at $2.2 \mu\text{m}$ that affects the near-IR bulge colors of some, but not all, NLS1 galaxies.

5.2. *Could The Mass-Luminosity Relation Hold For NLS1s?*

The alternative interpretation of our results is that the mass-luminosity relation does indeed hold for NLS1s and that the masses obtained from the correlation with broad-line radius are unreasonably low. It is evident from Figures 13 and 14 that the measured NLS1 bulge magnitudes are similar to those of the non-active galaxies used to derive the correlations. The estimates of M_{BH} for the NLS1s were obtained by interpolating within a region for which the correlations are known to be valid for broad-line Seyferts. This result is not in agreement with Botte et al. (2004), who suggest that the B -band luminosities of NLS1 bulges are lower than those of the broad line counterparts by approximately 1.3 magnitudes. However, as discussed earlier, near-IR wavelengths should in principle provide a more accurate trace of the underlying mass distribution than the B -band.

We are confident that our spectroscopic measurements do not suffer from any systematic errors. Therefore, if we accept the extension of the mass-luminosity relation to NLS1s, we require an explanation for the narrow emission lines that characterize these objects. Although strong non-virial motions in the broad-line region are known to induce asymmetries in the C IV line profiles in AGN spectra, their contribution at optical wavelengths is insufficient to significantly affect the $H\beta$ line profile (Véron-Cetty, Véron, & Gonçalves 2001). We have yet to directly resolve the broad line region, and rely on indirect evidence that the motion of the gas is virialized (Ferrarese & Ford 2005). If nuclear activity is triggered by galaxy mergers, the gas may be heavily influenced by non-gravitational forces, particularly at the earliest stages of the AGN duty cycle (e.g. Barnes & Hernquist 1991). It is possible that the broad-line emitting gas in the cores of NLS1s does not reflect only the gravitational potential of the central source. Departures from virialized motions would almost certainly broaden emis-

sion lines, increasing the discrepancy with the mass-luminosity relation.

As noted by Peterson et al. (2000), there are potential explanations for the remarkable spectral properties of NLS1s other than the low-mass hypothesis. It is possible that the orientation of the broad-line region could influence mass estimates derived using the Kaspi et al. (2005) relation. Studies of the central engines of active galaxies typically involve a large sample of objects with a range of spectral properties, and the assumption that the broad-line regions are oriented randomly does not affect the statistical results. On the other hand, NLS1s are a small and distinct subset of Seyfert galaxies, and the assumption of heterogeneity may not be reasonable. If NLS1 systems preferentially have a low inclination, values of M_{BH} could be underestimated by a factor of three or more.

In § 4.1, it was mentioned that the model geometry of the broad-line region could influence estimates of M_{BH} . An isotropic gas distribution is assumed in many studies that employ the mass-radius relation (e.g. Kaspi et al. 2000; Wandel 2002). The exclusion of a disk component in these studies could produce virial black-hole masses that are underestimated by a factor of three. As the two effects mentioned here are multiplicative, their net effect could lead to values of M_{BH} that are a full order of magnitude too low. Therefore, it is possible that our incongruent mass estimates are the result of the combined effects of broad-line geometry and orientation, and the mass-luminosity relation could indeed hold for NLS1s.

5.3. *Are NLS1s Fueled By Merger Events?*

Given the discrepancy between the estimates of M_{BH} revealed in this study, it is apparent that we cannot apply both the mass-radius and mass-luminosity relations to the NLS1 subset in the same form as used for broad-line AGN and non-active galaxies. The most common interpretation is a breakdown in the correlation with bulge luminosity. We have exercised a great deal of care in measuring accurate bulge magnitudes. We also have demonstrated that the application of the mass-radius relation to NLS1s may suffer from systematic effects that could lead to underestimated virial masses. Furthermore, we find no evidence for features that betray recent tidal interactions or distinct stellar components that would support the interpretation that NLS1s are evolutionarily young.

There may be an alternative view of NLS1s that provides an explanation for their exceptional properties, however. There are some interesting, albeit circumstantial, lines of evidence that point to a mechanism other than galaxy harassment to initiate accretion in these objects. It has been suggested that as the universe continues to expand and cosmic distances increase the role of mergers in defining galaxy morphology will become less important compared to secular evolution, the gradual reorganization of mass due to internal processes such as bar-driven instabilities (Kormendy & Kennicutt 2004). The photometric and kinematic properties of galaxies that have undergone secular evolution will be distinct and recognizable from those which arise from merger events. It is conceivable that NLS1s represent such objects.

The first piece of evidence in favor of this hypothesis involves the shape of the bulge surface brightness pro-

files. Bulges formed via secular evolution are believed to be more accurately represented by exponential profiles than by the de Vaucouleurs $r^{1/4}$ law (Balcells et al. 2003). When fitting the bulge components for the galaxies in our sample, the Sérsic index, n , was allowed to vary as a free parameter within the GALFIT minimization routine. The average of the optimal indices determined by GALFIT was 1.4 in K' and 1.6 in J , and n was never larger than 2.4. The NLS1 bulges were thus found to be more consistent with an exponential profile.

To be fair, the true nature of bulges remains somewhat ambiguous. In studying the bulge profiles of S0 to Sbc galaxies using the NICMOS near-IR camera on the Hubble Space Telescope, Balcells et al. (2003) found the average Sérsic index to be 1.7 ± 0.7 . Ground-based near-IR observations of the same sample were best fit by indices of 4 to 6. The authors suggest that the disagreement is caused by nuclear point source blending due to the effects of atmospheric seeing in the ground-based data. It is possible that this problem was mitigated in our ground-based data by the excellent angular resolution, combined with the application of our empirical technique for removing the nuclear emission.

Another key piece of evidence supporting secular evolution is the possible failure of the M_{BH} - σ_s correlation in NLS1s. Numerical simulations by Di Matteo, Springel, & Hernquist (2005) demonstrate that major galaxy mergers produce strong inflows of gas that feed the black hole. The energy emitted by the black hole expels gas from the central region, limiting star formation and regulating further accretion. The connection between M_{BH} and bulge velocity dispersion could therefore be a natural product of galaxy mergers. Conversely, the departure from this relationship by NLS1s may indicate that mergers are not largely responsible for initiating nuclear activity. Geometry may thus play a more significant role in the narrow $H\beta$ emission lines.

If accretion in NLS1s is not primarily the result of gravitational interactions, there must be an alternative mechanism for driving gas towards the nucleus. In the secular evolution paradigm, this is accomplished by stellar bars that produce non-axisymmetric gravitational potentials, driving gas inwards. Thus, barred early-type galaxies are ideal candidates for secular evolution (Kormendy & Kennicutt 2004). Interestingly, it was reported by Crenshaw, Kraemer & Gabel (2003) that large-scale bars appear to be more common in NLS1s than in broad-line AGN. Of the seven objects in our sample for which morphological information was available, four are classified as barred galaxies. We did not detect any such features in our near-IR data that could be included in the decompositions, however. Observations of early-type barred and unbarred systems by Aguerri et al. (2005) demonstrate that the presence of a bar does not change the galaxy morphological parameters such as Sérsic index and effective radius.

Given the arguments presented above, we postulate that NLS1s may represent AGN in which accretion may be regulated by internal processes rather than galaxy mergers. While there are outstanding issues that have not been addressed in this hypothesis, such as the x-ray properties of NLS1s and the exact cause of the narrow emission features, we feel that further investigation into

the possibility of secular development is warranted.

6. CONCLUSIONS

We have studied a sample of NLS1 galaxies in order to explore the hypothesis that such objects are evolutionarily young AGN possessing relatively low-mass black holes. Galaxy profiles were separated into their constituent components by applying the two-dimensional decomposition algorithm GALFIT to high-spatial resolution, near-IR imaging data. Black-hole masses were derived using the correlation between M_{BH} and host bulge luminosity, calibrated in J and K' using a sample of bright elliptical galaxies with black-hole masses obtained by resolving the sphere of influence. The scatter in the mass-luminosity relation was thus minimized by restricting the calibration sample to objects with secure M_{BH} estimates. Furthermore, the near-IR form of the relation is less sensitive to attenuation by dust than at optical wavelengths. The unweighted mean black-hole mass determined from this relation is, in solar units, $\langle \log(M_{BH}) \rangle = 7.9$, in line with typical values for broad-line Seyferts. We also derived masses for seven of the objects in our sample from the correlation between the radius of the broad-line region and the monochromatic continuum luminosity at 5100 Å under the assumption that the emission-line gas is virialized and using optical spectra taken from the literature. The mean mass calculated from this relation is $\langle \log(M_{BH}) \rangle = 6.4$, more consistent with the premise that the black holes in NLS1s are less massive than those found in their broad-line counterparts.

It is clear that there is a significant discrepancy between the results obtained from these correlations, with the mass-luminosity relation yielding values of M_{BH} that are on average more than one order of magnitude larger than those obtained from the mass-radius relation. Formal uncertainties in the calculated masses are typically around 0.25 dex, and thus are insufficient to account for the conflicting results. Our findings suggest that (at least) one of the correlations cannot be extended to the NLS1 subset in the same form as used for other galaxies. It has been conjectured that NLS1s may not follow the standard mass-luminosity relation due to contamination by circumnuclear star formation. We have argued that this extra component would not significantly affect our data. Furthermore, we noted that the resolution of our imaging data provided excellent spatial over-sampling of the surface brightness profiles, producing highly accurate bulge luminosities. The resulting M_{BH} estimates were calculated by interpolating the relation within a region known to be valid for both non-active galaxies and other AGN.

Numerical simulations of galaxy interactions constrain the high-accretion rate period that may define the start of the AGN duty cycle to a period shortly after a significant gravitational perturbation of the host galaxy. To further investigate this possibility, we compared the NLS1 bulge ($J-K_s$) color indices to a matched sample of non-active galaxies. We determined the mean bulge color for the NLS1 sample to be $\langle (J - K_s) \rangle = +1.85 \pm 0.58$. For the non-active galaxy sample, the mean color is $\langle (J - K_s) \rangle = +1.10 \pm 0.04$. Estimates of the bulge colors for broad-line Seyfert 1 galaxies were taken from the literature. A fair comparison to our sample

is complicated by the large scatter in the published results and the potential for misidentification of NLS1s as Seyfert 2 galaxies. The NLS1 images were also examined for light asymmetries or tidal features that may reflect a recent gravitational interaction. We find no evidence for any significant morphological asymmetries or extra stellar components that would suggest these galaxies are evolutionarily young.

We have, however, identified several lines of circumstantial evidence suggesting that nuclear fueling in NLS1s may be strongly influenced by secular processes within the host galaxy. The bulge light profiles obtained from our two-dimensional decompositions are all nearly exponential in shape, a key characteristic of secular evolution. NLS1s may not follow the standard $M_{BH}-\sigma_s$ relation, which has been shown to be a natural product of galaxy mergers, while an enhanced fraction of stellar bar structures in NLS1s may provide a natural source for fueling the nucleus without invoking a recent gravitational interaction. It is thus fair to acknowledge that we do not yet completely understand the evolution of this important subset of low-redshift active galaxies.

ACKNOWLEDGMENTS.

The authors would like to thank the anonymous referee for insightful comments that improved our manuscript. The authors would also like to thank the Natural Sciences and Engineering Research Council of Canada and the CFHT TAC for supporting this work, and X.Y. Dong for insightful discussions. This publication makes use of data products from the Two Micron All Sky Survey, which is a joint project of the University of Massachusetts and the Infrared Processing and Analysis Center/California Institute of Technology, funded by the National Aeronautics and Space Administration and the National Science Foundation. This research has made use of the NASA/IPAC Extragalactic Database (NED) which is operated by the Jet Propulsion Laboratory, California Institute of Technology, under contract with the National Aeronautics and Space Administration.

REFERENCES

- Aguerri, J.A.L., Elias-Rosa, N., Corsini, E.M., & Muñoz-Tuñón, C. 2005, *A&A*, 434, 109
- Andredakis, Y.C., Peletier, R.F., & Balcells, M. 1995, *MNRAS*, 275, 874
- Balcells, M., Graham, A.W., Domínguez-Palmero, & Peletier, R.F. 2003, *ApJ*, 582, L79
- Barnes, J.E. & Hernquist, L.E. 1991, *ApJ*, 370, L65
- Barth, A.J., Greene, J.E., & Ho, L.C. 2005, *ApJ*, 619, L151
- Bender, R., et al. 2005, *ApJ*, 631, 280
- Beuzit, J.-L. & Hainaut, M.-C. 1998, User's Manual for the CFHT Adaptive Optics Bonnette, v0.9, The Canada-France-Hawaii Telescope Corporation
- Bian, W. & Zhao, Y. 2004, *MNRAS*, 347, 607
- Boller, Th., Brandt, W.N., & Fink, H. 1996, *A&A*, 305, 53
- Borosen, T.A. & Green, R.F. 1992, *ApJS*, 80, 109
- Botte, V., Ciroti, S., Rafanelli, P., & Di Mille, F. 2004, *AJ*, 127, 3168
- Caon, N., Capaccioli, M., & D'Onofrio, M. 1993, *MNRAS*, 265, 1013
- Crenshaw, D.M., Kraemer, S.B., & Gabel, J.R. 2003, *AJ*, 126, 1690
- de Vaucouleurs, G. 1948, *Ann. Astrophys.*, 11, 247
- de Vaucouleurs, G., de Vaucouleurs, A., Corwin, H.G., Buta, R.J., Paturel, G., & Fouque, P. 1991, *Third Reference Catalogue of Bright Galaxies* (New York: Springer-Verlag)
- Di Matteo, T., Springel, V., & Hernquist, L. 2005, *Nature*, 433, 604
- Dong, X.Y. & De Robertis, M.M. 2006, *AJ*, 131, 1236
- Falcón-Barroso, J., Peletier, R.F., & Balcells, M. 2002, *MNRAS*, 335, 741
- Ferrarese, L. & Ford, H. 2005, *Space Sci. Rev.*, 116, 523
- Ferrarese, L. & Merritt, D. 2000, *ApJ*, 539, L9
- Fioc, M. & Rocca-Volmerange, B. 1999, *A&A*, 351, 869
- Freeman, K.C. 1970, *ApJ*, 160, 811
- Gebhardt, K., et al. 2000, *ApJ*, 539, L13
- Graham, A.W. 2001, *AJ*, 121, 820
- Greene, J.E. & Ho, L.C. 2005a, *ApJ*, 627, 721
- Greene, J.E. & Ho, L.C. 2005b, *ApJ*, 630, 122
- Grupe, D. & Mathur, S. 2004, *ApJ*, 606, L41
- Grupe, D., Wills, B.J., Leighly, K.M., & Meusinger, H. 2004, *AJ*, 127, 156
- Haehnelt, M.G. & Rees, M.J. 1993, *MNRAS*, 263, 168
- Håring, N. & Rix, H.-W. 2004, *ApJ*, 604, L89
- Hunt, L.K., Malkan, M.A., Salvati, M., Mandolesi, N., Palazzi, E., & Wade, R. 1997, *ApJS*, 108, 229
- Kaspi, S., Maoz, D., Netzer, H., Peterson, B.M., Vestergaard, M., & Jannuzi, B.T. 2005, *ApJ*, 629, 61
- Kaspi, S., Smith, P.S., Netzer, H., Maoz, D., Jannuzi, B.T., & Giveon, U. 2000, *ApJ*, 533, 631
- Kim, S.S., Figer, D.F., Lee, M.G., & Oh, S. 2005, *PASP*, 117, 445
- Kormendy, J. & Illingworth, G. 1982, *ApJ*, 256, 460
- Kormendy, J. & Kennicutt, R.C. 2004, *ARA&A*, 42, 603
- Kormendy, J. & Richstone, D. 1995, *ARA&A*, 33, 581
- Laor, A. 2001, *ApJ*, 553, 677
- Liu, C.T. & Kennicutt, R.C. 1995, *ApJ*, 450, 547
- Magorrian, J., et al. 1998, *AJ*, 115, 2285
- Marconi, A. & Hunt, L.K. 2003, *ApJ*, 589, L21
- Márquez et al. 2000, *A&A*, 360, 431
- Mathis, J.S. 1990, *ARA&A*, 28, 37
- Mathur, S. 2000, *MNRAS*, 314, L17
- Mathur, S., Kuraszewicz, J., & Czerny, B. 2001, *NewA*, 6, 321
- McLure, R.J. & Dunlop, J.S. 2001, *MNRAS*, 327, 199
- Nelson, C.H., Green, R.F., Bower, G., Gebhardt, K., & Weistrop, D. 2004, *ApJ*, 615, 652
- Osterbrock, D.E. 1993, *ApJ*, 404, 551
- Osterbrock, D.E. & Pogge, R.W. 1985, *ApJ*, 297, 166
- Peng, C.Y., Ho, L.C., Impey, C.D., & Rix, H.-W. 2002, *AJ*, 124, 266
- Peterson, B.M. & Wandel, A. 2000, *ApJ*, 540, L13
- Peterson, B.M., et al. 2000, *ApJ*, 542, 161
- Poggianti, B.M. 1997, *A&A*, 122, 399
- Pounds, K.A., Done, C., & Osborne, J. 1995, *MNRAS*, 277, L5
- Press, W.H., Teukolsky, S.A., Vetterling, W.T., & Flannery, B.P. 1992, *Numerical Recipes in C* (2nd Ed.; Cambridge: Cambridge Univ. Press)
- Rees, M.J. 1984, *ARA&A*, 22, 471
- Rigaut, F., et al. 1998, *PASP*, 110, 152
- Rodríguez-Ardila, A., Contini, M., & Viegas, S.M. 2005, *MNRAS*, 357, 220
- Rodríguez-Ardila, A. & Mazzalay, X. 2006, *MNRAS*, 367, L57
- Rudy, R.J., Mazuk, S., Puetter, R.C., & Hamann, F. 2000, *ApJ*, 539, 166
- Schlegel, D.J., Finkbeiner, D.P., & Davis, M. 1998, *ApJ*, 500, 525
- Sérsic, J.L. 1968, *Atlas de galaxias australes*. Observatorio Astronomico, Cordoba
- Shemmer, O., et al. 2001, *ApJ*, 561, 162
- Simien, F. & de Vaucouleurs, G. 1986, *ApJ*, 302, 564
- Sulentic, J.W., Zwitter, T., Marziani, P., & Dultzin-Hacyan, D. 2000, *ApJ*, 536, L5
- Tonry, J.L., Dressler, A., Blakeslee, J.P., Ajhar, E.A., Fletcher, A.B., Luppino, G.A., Metzger, M.R., & Moore, C.B. 2001, *ApJ*, 546, 681
- Vaduvescu, O. & McCall, M.L. 2004, *PASP*, 116, 640
- Vanzi, L., Alonso-Herrero, A., & Rieke, G.H. 1998, *ApJ*, 504, 93
- Véron-Cetty, M.-P. & Véron, P. 2001, *A&A*, 374, 92
- Véron-Cetty, M.-P., Véron, P., & Gonçalves, A.C. 2001, *A&A*, 372, 730
- Virani, S.N., De Robertis, M.M., & VanDalsen, M.L. 2000, *AJ*, 120, 1739
- Wainscoat, R.J. & Cowie, L.L. 1992, *AJ*, 103, 332
- Wandel, A. 2002, *ApJ*, 565, 762
- Wang, T. & Lu, Y. 2001, *A&A*377, 52
- Williams, R.J., Pogge, R.W., & Mathur, S. 2002, *AJ*, 124, 3042
- York, D.G. et al. 2000, *AJ*, 120, 1579

TABLE 1
NLS1 GALAXY PARAMETERS

Target ID	Distance ^a (Mpc)	Morph. Class.	Total Magnitude ^b		Optical SMA (arcsec)	$K=+20$ Isophotal Radius (arcsec)
			J	K_s		
Mrk 335	111.1	S0/a	+12.03 ± 0.04	+10.06 ± 0.03	9	15.1
Mrk 359	74.8	SB0a	+11.61 ± 0.02	+10.46 ± 0.03	18	16.6
Mrk 618	153.6	SB(s)b pec	+11.82 ± 0.03	+10.37 ± 0.03	27	18.1
Mrk 705	125.7	S0?	+11.94 ± 0.03	+10.74 ± 0.04	21	16.1
Mrk 734	217.6	Compact	+13.04 ± 0.04	+11.76 ± 0.06	18	7.6
Mrk 1044	70.7	SB0	+11.78 ± 0.03	+10.47 ± 0.03	21	14.0
Mrk 1126	45.7	(R)SB(r)a	+11.09 ± 0.02	+10.14 ± 0.04	54	26.1
Mrk 1239	85.8	E-S0	+11.87 ± 0.02	+9.60 ± 0.02	12	10.1
IRAS 04596-2257	176.5	-	+13.21 ± 0.04	+12.03 ± 0.06	9.3	6.4
MCG 08.15.009	105.0	-	+12.42 ± 0.05	+11.28 ± 0.07	18	14.1
PG 1016+336	105.6	Compact	+13.03 ± 0.05	+11.67 ± 0.06	9	11.6

^aDistances were calculated using redshift information obtained from the literature.

^bTotal galaxy magnitudes and isophotal radii at $K = +20$ are taken from the 2MASS XSC; optical radii are taken from the literature.

TABLE 2
SUMMARY OF OBSERVATIONS

Target ID	Coordinates		Exposure Time ^a		Mean Airmass	
	R.A. (J2000)	Decl. (J2000)	J	K'	J	K'
Mrk 335	00 06 19.5	+20 12 10.5	1200	80	1.18	1.08
Mrk 359	01 27 32.6	+19 10 43.8	1200	480	1.04	1.13
Mrk 618	04 36 22.2	-10 22 33.8	1200	120	1.17	1.16
Mrk 705	09 26 03.3	+12 44 03.6	1680	480	1.04	1.14
Mrk 734	11 21 47.1	+11 44 18.3	480	240	1.01	1.02
Mrk 1044	02 30 05.4	-08 59 52.6	1920	480	1.16	1.27
Mrk 1126	23 00 47.8	-12 55 06.7	1680	1680	1.40	1.63
Mrk 1239	09 52 19.1	-01 36 43.5	480	240	1.09	1.09
IRAS 04596-2257	05 01 48.6	-22 53 23.2	1680	1920	1.41	1.44
MCG 08.15.009	07 51 51.9	+49 48 51.6	1920	1920	1.16	1.16
PG 1016+336	10 19 49.5	+33 22 03.7	1680	480	1.03	1.04

NOTE. — Units of right ascension are hours, minutes, and seconds; units of declination are degrees, arcminutes, and arcseconds.

^aExposure times represent total on-target integration time.

TABLE 3
PHOTOMETRIC AND STRUCTURAL PARAMETERS OF COMPONENTS

Target ID	J -band Results					K_s -band Results				
	$M(\text{bulge})^a$	$M(\text{disk})$	B/D	Sérsic n	r (kpc) ^b	$M(\text{bulge})$	$M(\text{disk})$	B/D	Sérsic n	r (kpc)
Mrk 335 [†]	-21.29	-21.69	0.70	1.02	0.25	-23.33	-22.91	1.43	1.23	0.15
Mrk 359	-20.42	-22.38	0.16	1.92	0.23	-22.40	-23.97	0.24	2.13	0.23
Mrk 618	-21.74	-23.01	0.31	1.20	0.22	-23.83	-27.00	0.05	1.55	0.26
Mrk 705 [†]	-22.47	-24.66	0.13	2.40	0.93	-23.97	-25.87	0.17	2.28	0.54
Mrk 734 [†]	-22.34	-25.58	0.05	2.10	0.60	-23.82	-24.32	0.63	1.47	0.33
Mrk 1044	-20.78	-21.35	0.59	0.96	0.23	-22.83	-22.49	1.36	0.83	0.17
Mrk 1126	-20.15	-22.59	0.11	1.64	0.29	-21.35	-22.72	0.29	1.75	0.21
Mrk 1239	-21.72	-22.63	0.43	1.65	0.17	-24.76	-25.60	0.46	1.08	0.19
IRAS 04596-2257	-21.42	-21.90	0.64	1.16	0.37	-23.56	-23.49	1.08	0.81	0.60
MCG 08.15.009	-21.70	-	-	1.45	1.02	-22.66	-	-	1.15	0.56
PG 1016+336	-20.41	-21.06	0.55	1.27	0.19	-22.32	-22.05	1.29	0.94	0.12

NOTE. — Galaxies with multiple image sets acquired in K_s are denoted by [†]. For these objects, the mean fit parameters are listed.

^aAbsolute magnitudes of galaxy components derived from GALFIT output.

^bBulge scale radius in kpc.

TABLE 4
GALAXIES USED TO CALIBRATE MASS-LUMINOSITY RELATION.

Object	Distance ^a (Mpc)	M_{BH} ($10^8 M_{\odot}$)	M_J	M_{K_s}
IC 1459	28.8	26.0 ± 11.0	-24.62 ± 0.28	-25.50 ± 0.28
NGC 221	0.77	0.025 ± 0.005	-18.21 ± 0.08	-19.36 ± 0.08
NGC 3377	10.9	$1.00^{+0.9}_{-0.1}$	-21.93 ± 0.09	-22.76 ± 0.09
NGC 3379	10.3	1.35 ± 0.73	-22.93 ± 0.11	-23.81 ± 0.11
NGC 3608	22.5	$1.9^{+1.0}_{-0.6}$	-22.83 ± 0.14	-23.67 ± 0.14
NGC 4261	31.1	5.4 ± 1.2	-24.28 ± 0.19	-25.21 ± 0.19
NGC 4291	25.3	$3.1^{+0.8}_{-2.3}$	-22.69 ± 0.32	-23.62 ± 0.32
NGC 4374	17.7	$17^{+12}_{-6.7}$	-24.15 ± 0.11	-25.04 ± 0.11
NGC 4473	15.3	$1.1^{+0.5}_{-0.8}$	-22.91 ± 0.13	-23.78 ± 0.13
NGC 4486	15.8	35.7 ± 10.2	-24.29 ± 0.16	-25.18 ± 0.16
NGC 4564	14.5	$0.56^{+0.03}_{-0.08}$	-21.97 ± 0.17	-22.89 ± 0.17
NGC 4649	16.4	$20.0^{+4.0}_{-6.0}$	-24.43 ± 0.15	-25.35 ± 0.15
NGC 4697	11.4	$1.7^{+0.2}_{-0.3}$	-23.08 ± 0.14	-23.94 ± 0.14
NGC 5845	24.7	$2.4^{+0.4}_{-1.4}$	-21.94 ± 0.21	-22.88 ± 0.21
NGC 6251 [†]	99.4	5.9 ± 2.0	-25.01 ± 0.22	-25.99 ± 0.22
NGC 7052 [†]	62.5	$3.7^{+2.6}_{-1.5}$	-24.55 ± 0.22	-25.45 ± 0.22

^aGalaxy distances obtained from Tonry et al. (2001) except for two objects denoted by [†]. Distances for these galaxies determined using redshift information from the RC3.

TABLE 5
BLACK HOLE MASS ESTIMATES

Target ID	FWHM(H β) ^a (km s ⁻¹)	$\lambda L_{\lambda}(5100 \text{ \AA})$ (10 ⁴⁴ erg s ⁻¹)	$L(\text{H}\beta)$ (10 ⁴² erg s ⁻¹)	log M_{BH} (Mass-Radius Relation) ^b		log M_{BH} (Mass-Luminosity Relation)		
				$L_{\lambda}(5100 \text{ \AA})$	$L(\text{H}\beta)$	J-band	K_s -band	T Type
Mrk 335	1640	0.640 \pm 0.006	1.0 \pm 0.1	6.81	6.99	7.64	8.12	8.37
Mrk 359	480	0.193 \pm 0.004	0.07 \pm 0.01	5.38	5.28	7.27	7.71	7.82
Mrk 618	2300	-	-	-	-	7.83	8.34	8.31
Mrk 705	1990	0.273 \pm 0.004	0.33 \pm 0.04	6.72	6.88	8.15	8.40	8.26
Mrk 734	1820	0.728 \pm 0.007	0.6 \pm 0.1	6.94	6.94	8.09	8.33	-
Mrk 1044	1280	0.153 \pm 0.003	0.19 \pm 0.02	6.17	6.36	7.42	7.90	7.76
Mrk 1126	2500	-	-	-	-	7.15	7.25	7.49
Mrk 1239	910	0.163 \pm 0.004	0.24 \pm 0.04	5.89	6.13	7.83	8.75	8.41
IRAS 04596-2257	1500	-	-	-	-	7.70	8.22	-
MCG 08.15.009	-	-	-	-	-	7.82	7.82	7.92
PG 1016+336	1600	0.073 \pm 0.001	0.059 \pm 0.006	6.14	6.28	7.26	7.68	7.61
Average				6.29	6.41	7.65	8.05	7.99

^aValues for the FWHM of the broad component of H β taken from Véron-Cetty, Véron, & Gonçalves (2001).

^bBlack-hole masses are presented in log space, in units of solar masses.

TABLE 6
NON-ACTIVE GALAXY PARAMETERS

Target ID	Distance ^a (Mpc)	<i>J</i> -band Results		<i>K_s</i> -band Results	
		<i>M</i> (bulge) ^b	<i>M</i> (disk)	<i>M</i> (bulge)	<i>M</i> (disk)
IC 356	18.1	-22.83	-24.29	-23.81	-25.12
IC 520	47.0	-22.50	-23.32	-23.48	-24.22
NGC 266	62.4	-21.85	-24.08	-23.31	-24.88
NGC 2146	17.2	-22.42	-22.10	-24.06	-21.47
NGC 2775	17.0	-21.08	-23.10	-22.28	-23.91
NGC 2782	37.3	-21.28	-22.61	-22.56	-23.32
NGC 2985	22.4	-22.81	-22.59	-23.77	-23.41
NGC 3166	22.0	-21.83	-22.64	-22.92	-23.40
NGC 3169	19.7	-22.74	-22.34	-23.82	-22.93
NGC 3190	22.4	-21.76	-22.41	-22.94	-23.47
NGC 3504	26.5	-21.40	-22.60	-22.61	-23.44
NGC 3583	34.0	-20.46	-22.33	-21.69	-23.42
NGC 3705	17.0	-21.36	-21.11	-22.40	-21.88
NGC 3729	17.0	-18.90	-20.79	-20.06	-21.65
NGC 3884	91.6	-22.46	-24.20	-23.46	-25.13
NGC 3898	21.9	-22.47	-22.28	-23.43	-23.10
NGC 4064	16.9	-20.31	-21.38	-21.49	-22.05
NGC 4192	16.8	-20.87	-23.21	-22.11	-24.07
NGC 4293	17.0	-19.59	-21.73	-20.91	-22.76
NGC 4369	21.6	-20.34	-21.63	-21.30	-22.44
NGC 4457	17.4	-21.79	-21.97	-22.80	-22.68
NGC 4643	25.7	-23.58	-22.11	-24.49	-23.07
NGC 4665	17.9	-21.13	-22.67	-22.07	-23.44
NGC 5377	31.0	-21.95	-22.85	-22.96	-23.68
NGC 5701	26.1	-23.25	-20.66	-24.08	-21.97
NGC 6340	22.0	-20.78	-22.21	-21.72	-23.03
NGC 6654	29.5	-21.41	-22.60	-22.37	-23.47

^aDistances were calculated using redshift information obtained from the literature.

^bAbsolute magnitudes of components derived from GALFIT model fits to 2MASS data.

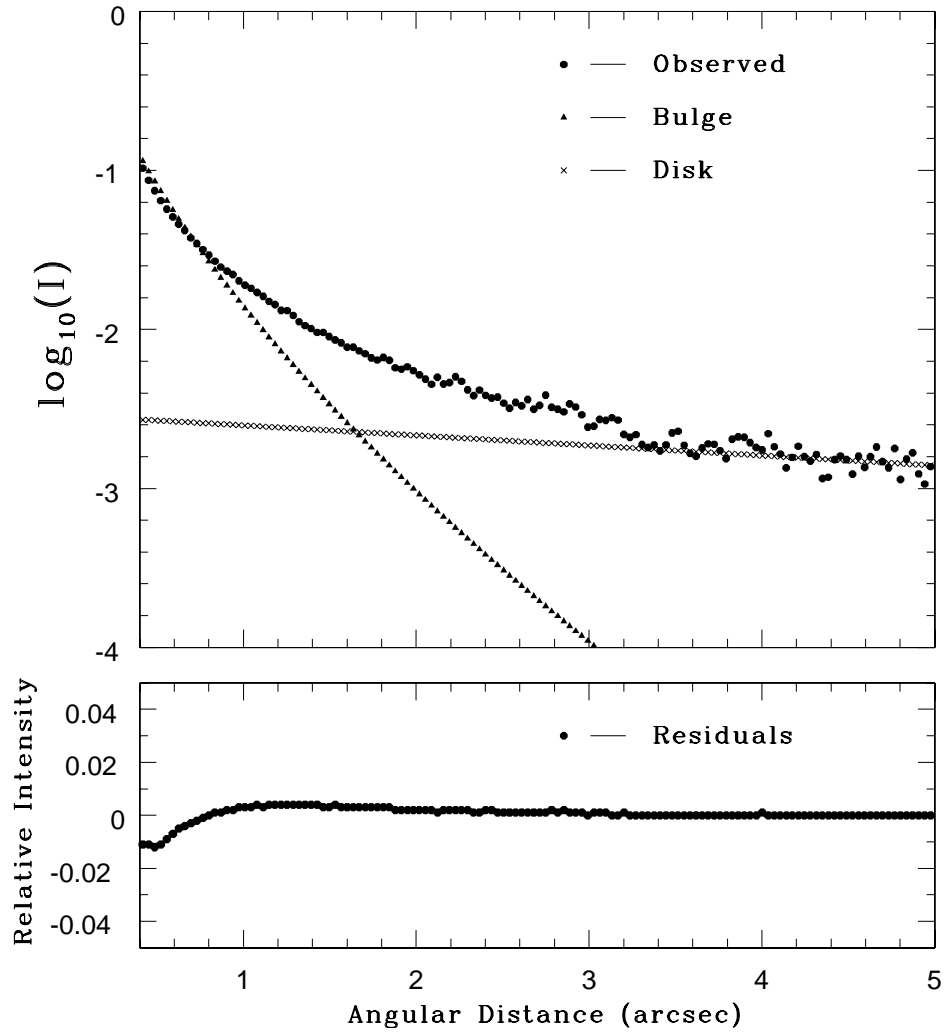
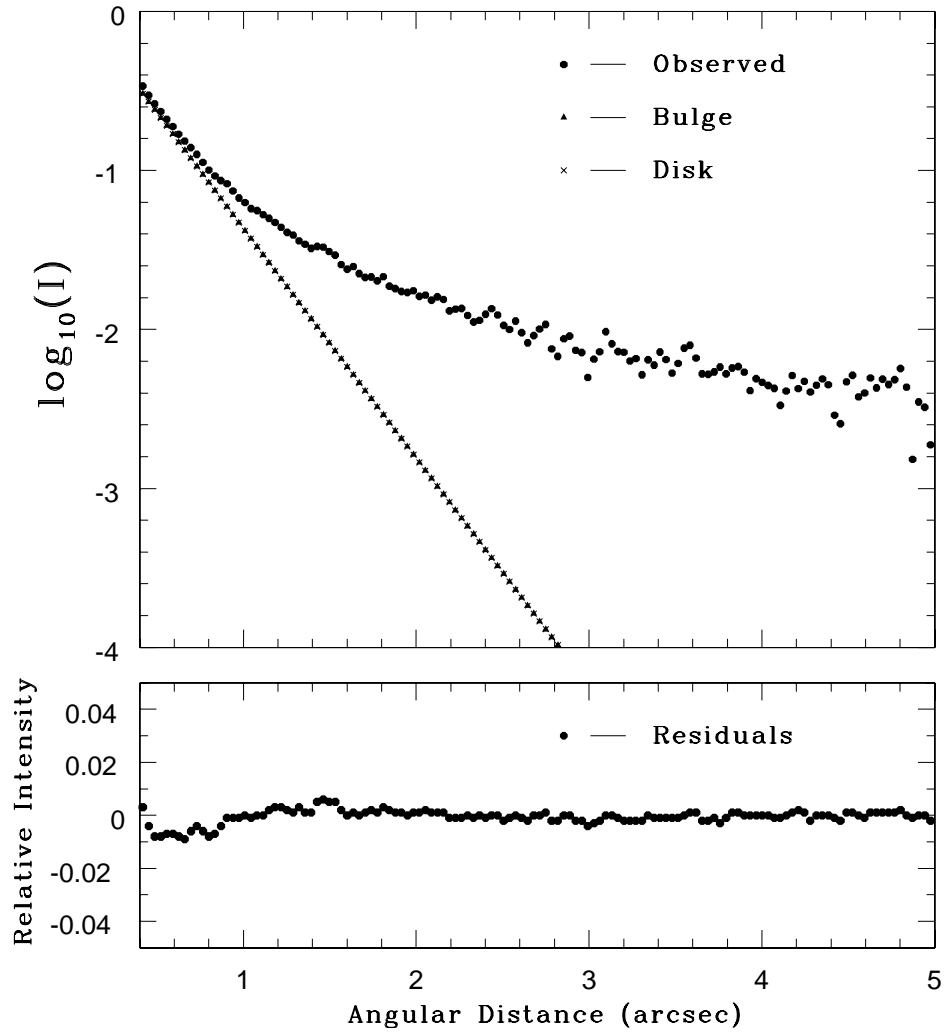
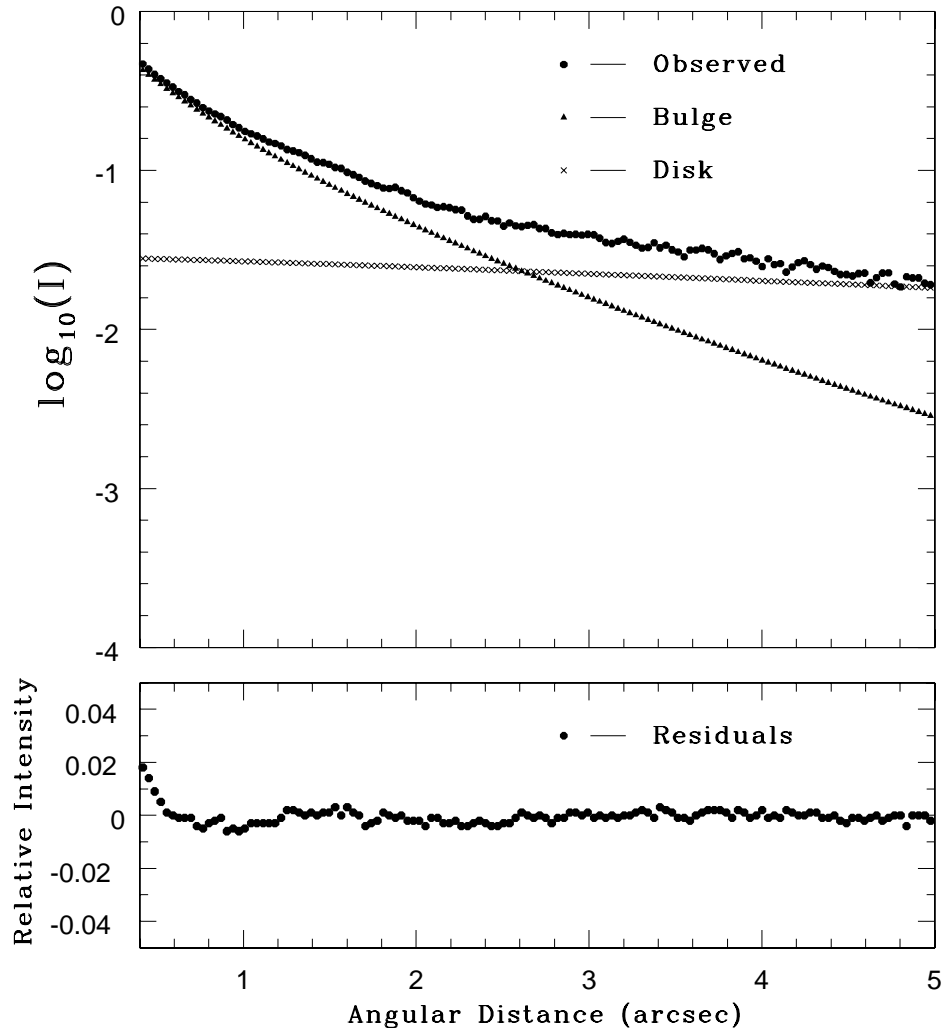
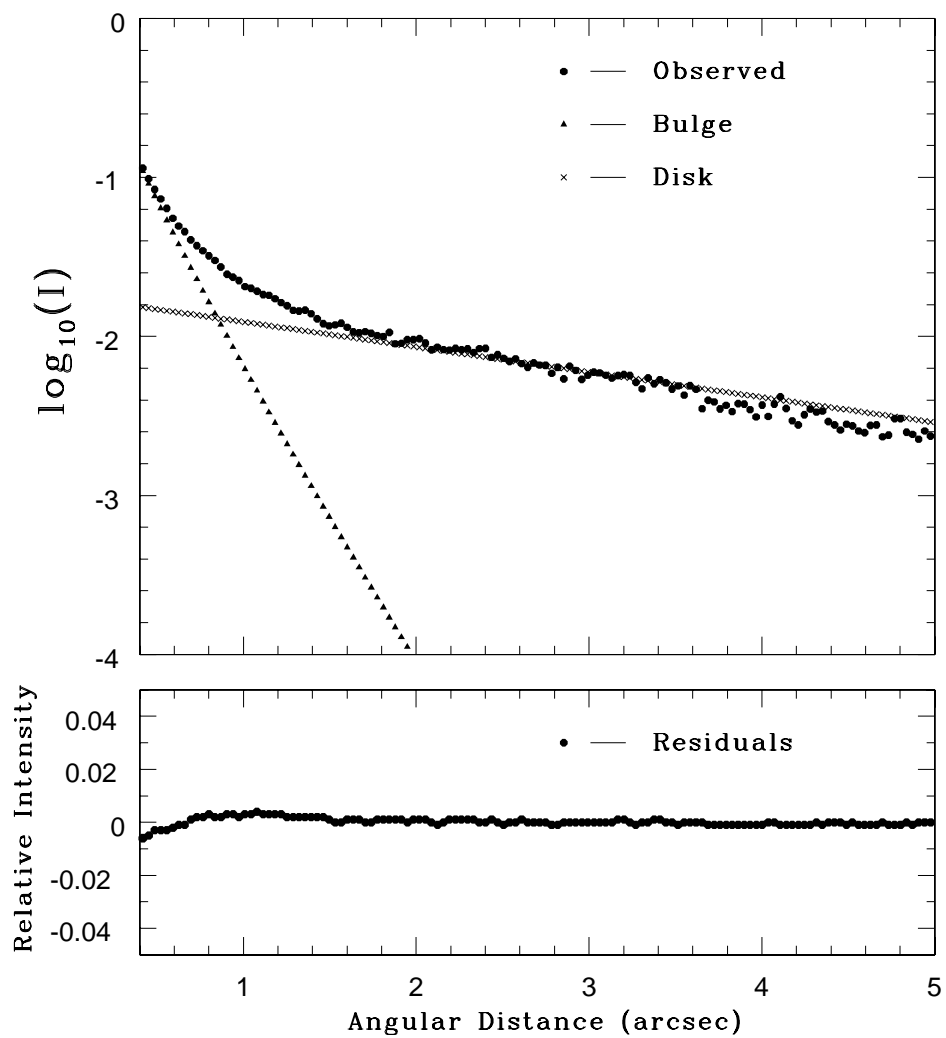
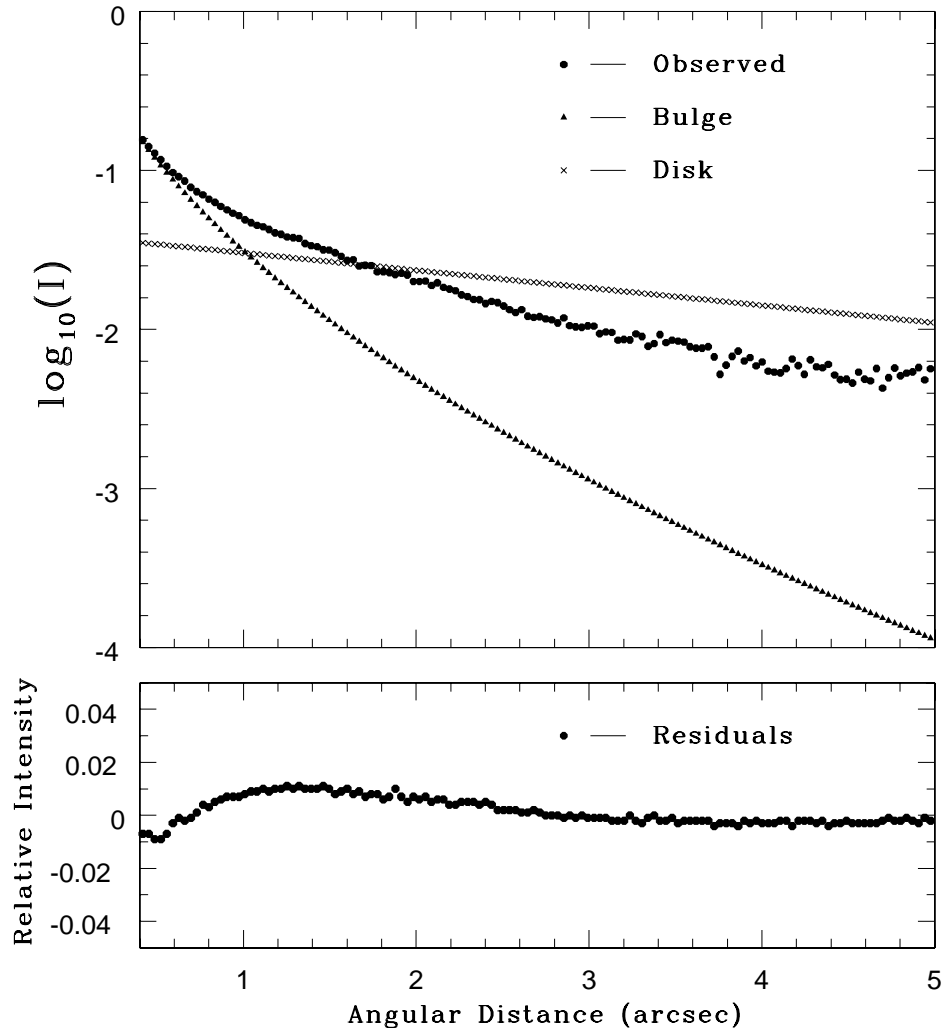


FIG. 1.— *J*-band surface brightness profile for Mrk 1239. The top panel shows the relative contribution of each component. In the lower panel, the residuals (observation minus model) are plotted.

FIG. 2.— J -band surface brightness profile for Mrk 335.

FIG. 3.— *J*-band surface brightness profile for Mrk 1126.

FIG. 4.— *J*-band surface brightness profile for Mrk 618.

FIG. 5.— J -band surface brightness profile for Mrk 359.

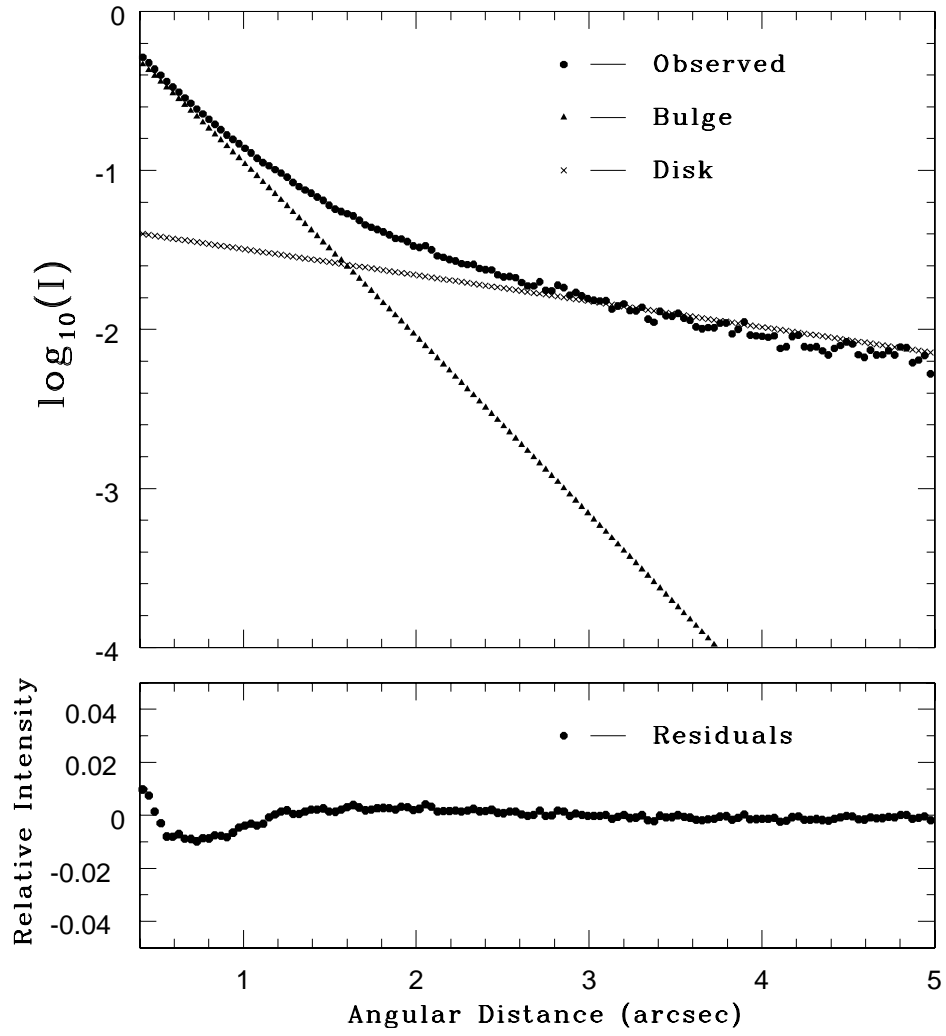
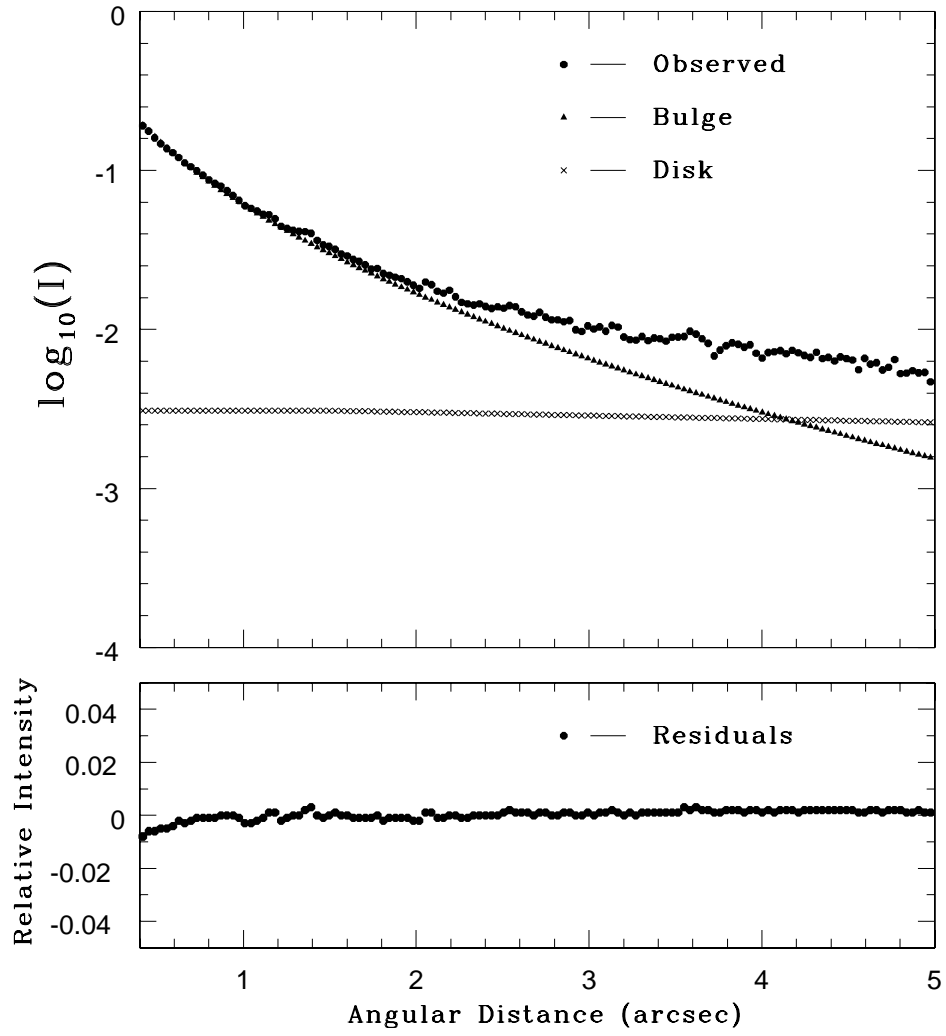


FIG. 6.— *J*-band surface brightness profile for Mrk 1044.

FIG. 7.— J -band surface brightness profile for Mrk 705.

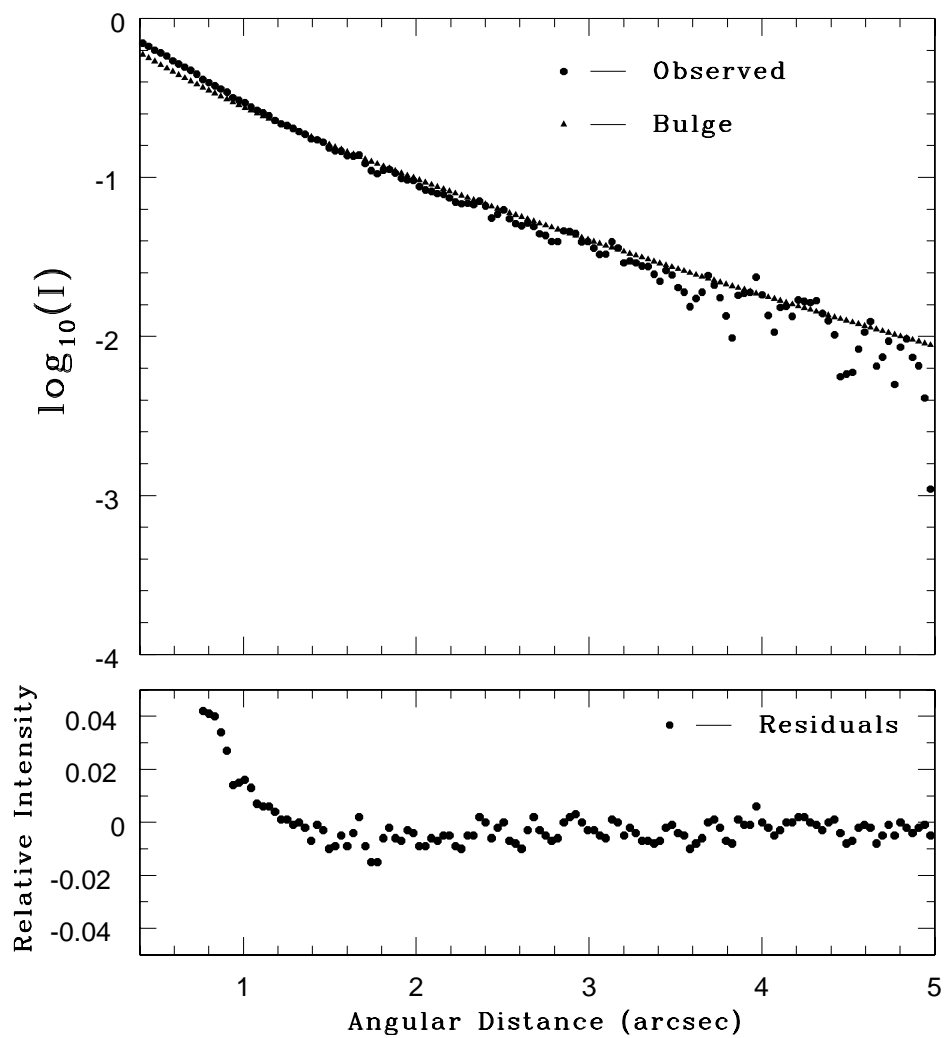
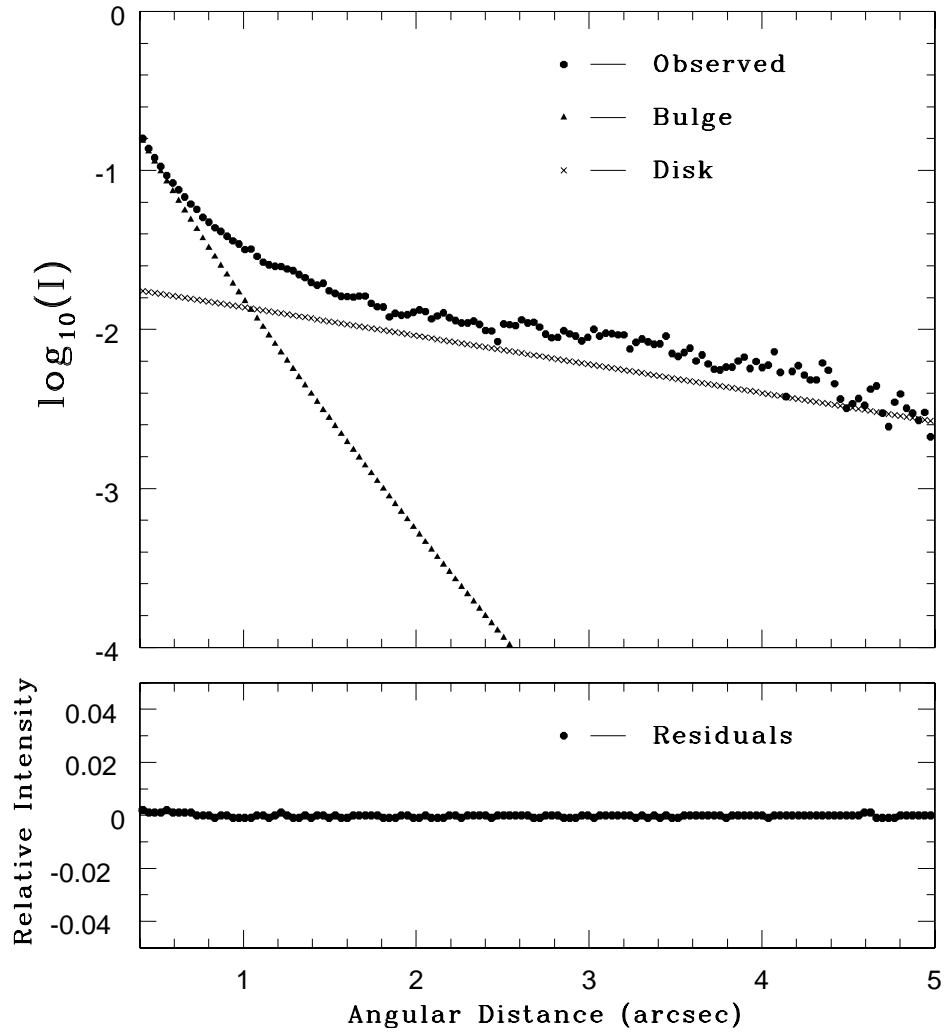
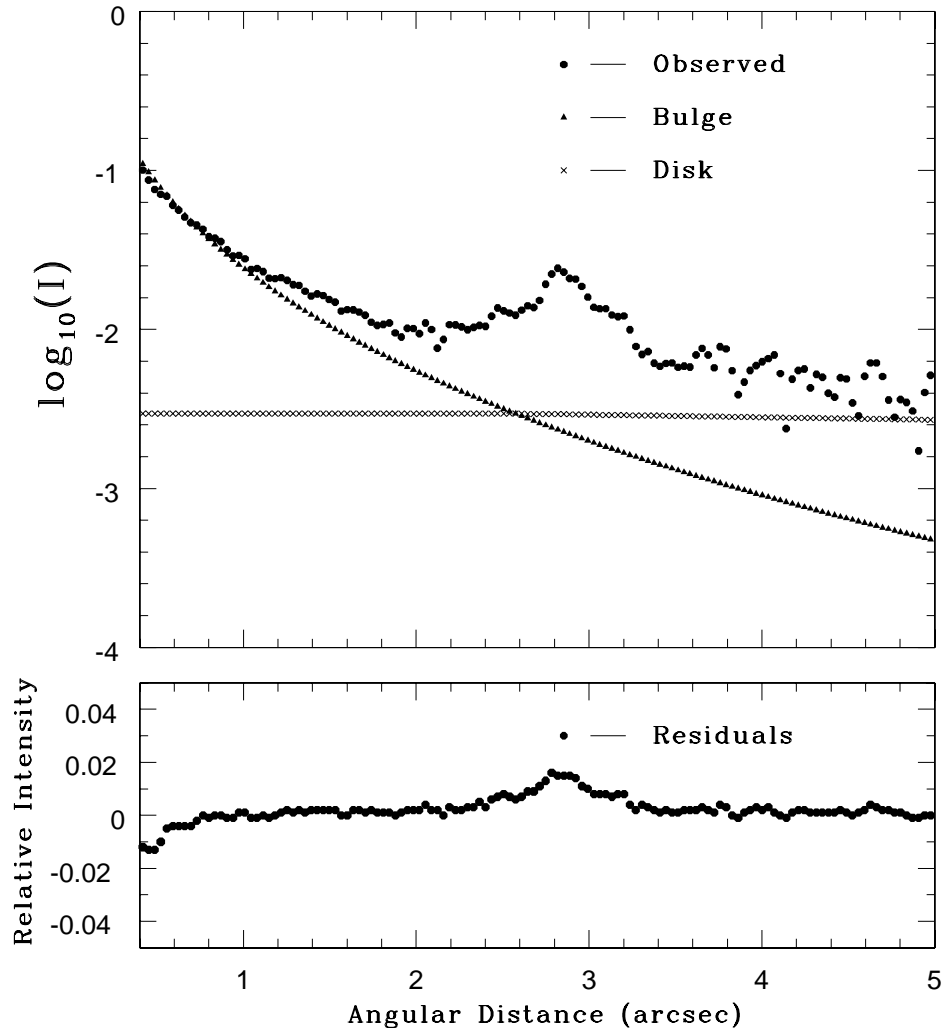
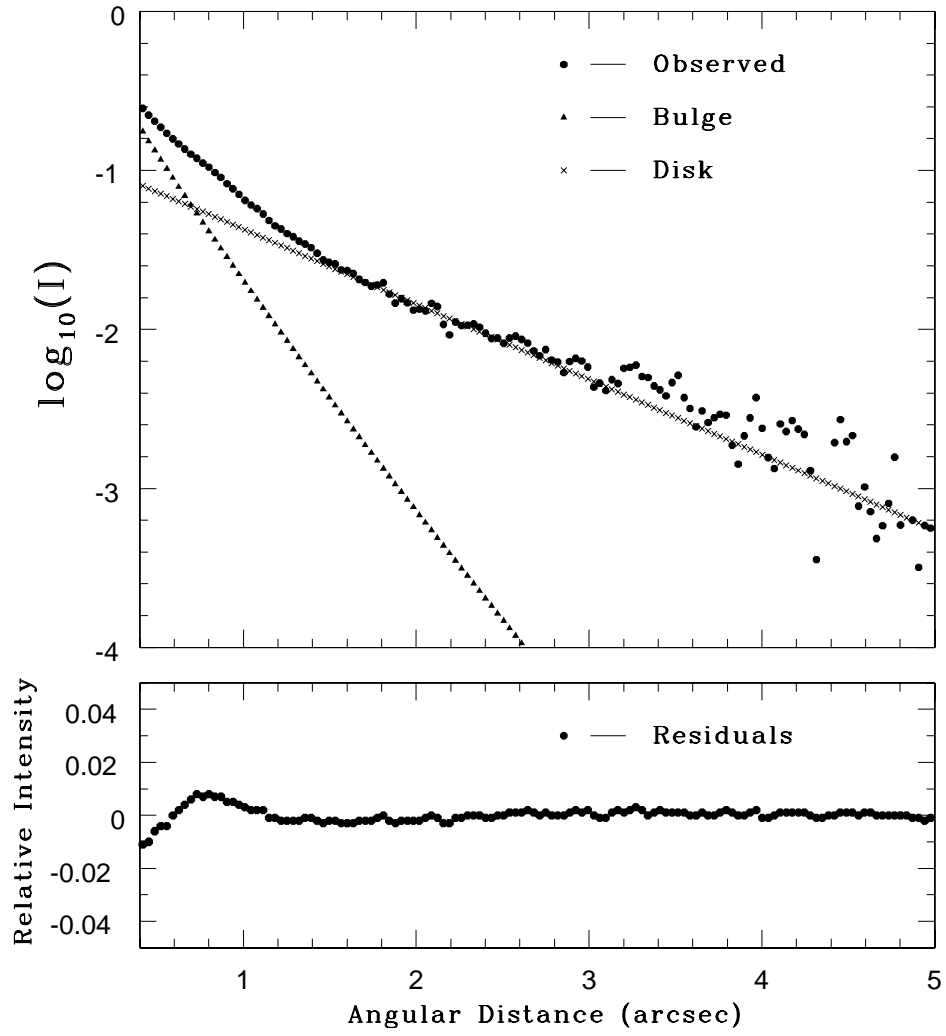


FIG. 8.— J -band surface brightness profile for MCG 08.15.009.

FIG. 9.— *J*-band surface brightness profile for PG 1016+336.

FIG. 10.— *J*-band surface brightness profile for Mrk 734.

FIG. 11.— *J*-band surface brightness profile for IRAS 04596-2257.

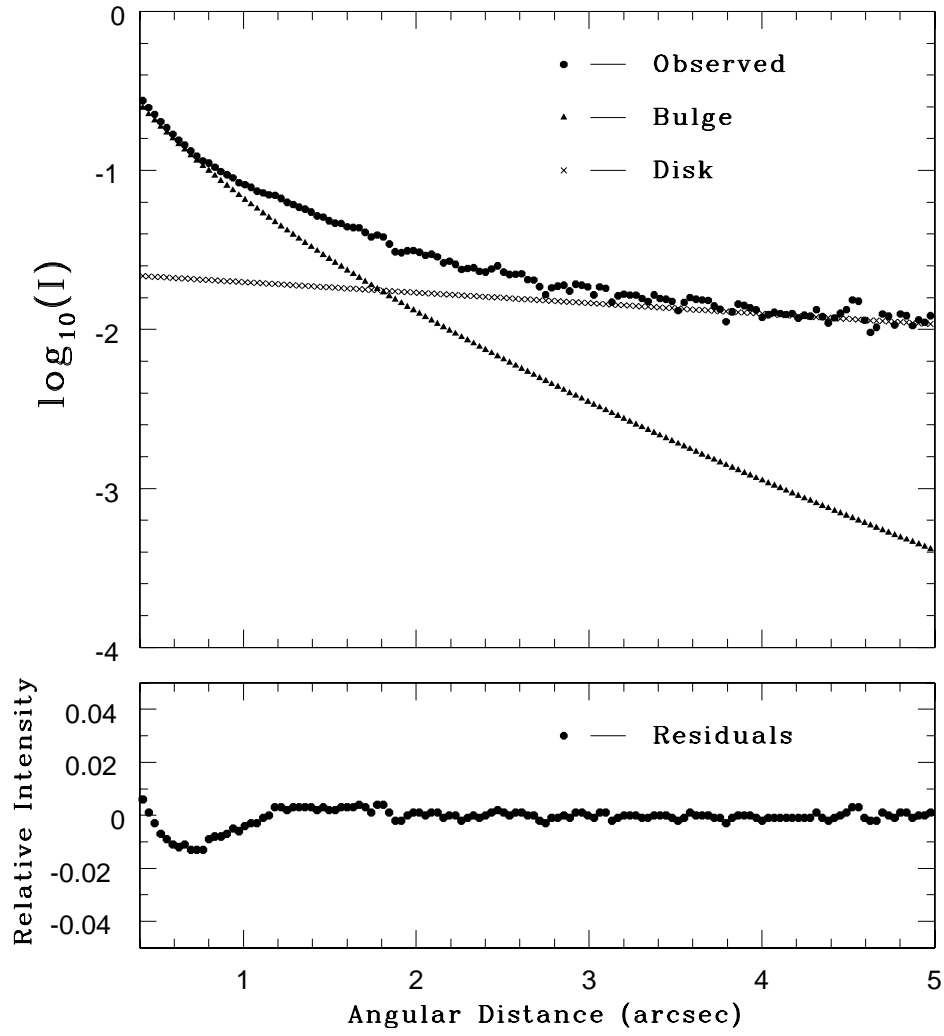


FIG. 12.— K_s -band surface brightness profile for Mrk 1126, illustrating the residual pattern seen near the centers of many of the model fits in K_s .

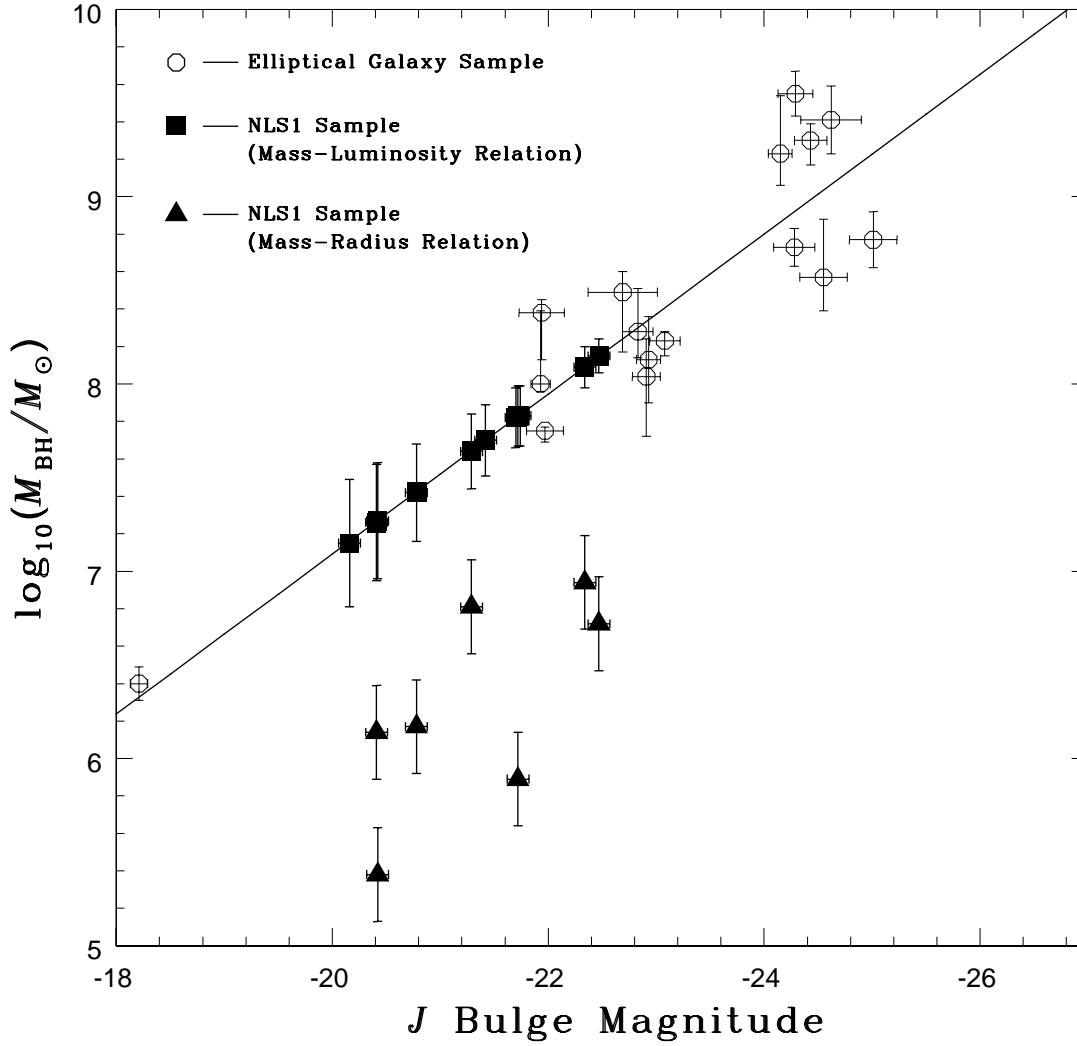


FIG. 13.— Correlation between black hole mass and host galaxy bulge luminosity, calibrated for J -band data. Open circles (colored blue in electronic edition) denote elliptical galaxies with secure estimates of M_{BH} . NLS1 mass estimates computed using this correlation are plotted as (red) squares. NLS1 black-hole masses derived using the mass-radius relation are denoted by (green) triangles. The (blue) solid line represents the weighted linear least-squares fit to the elliptical galaxy data.

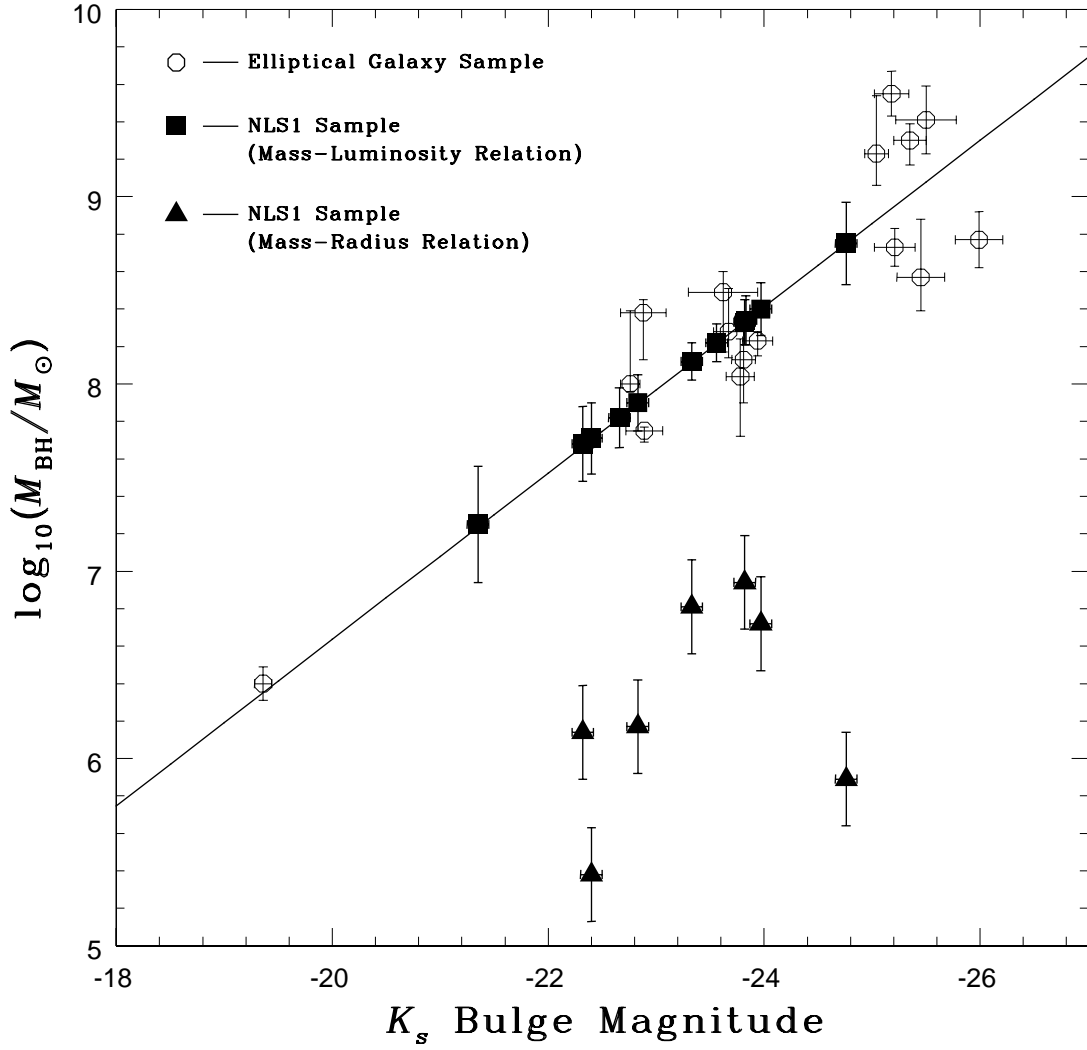


FIG. 14.— Correlation between black hole mass and host bulge luminosity, calibrated for K_s -band data.

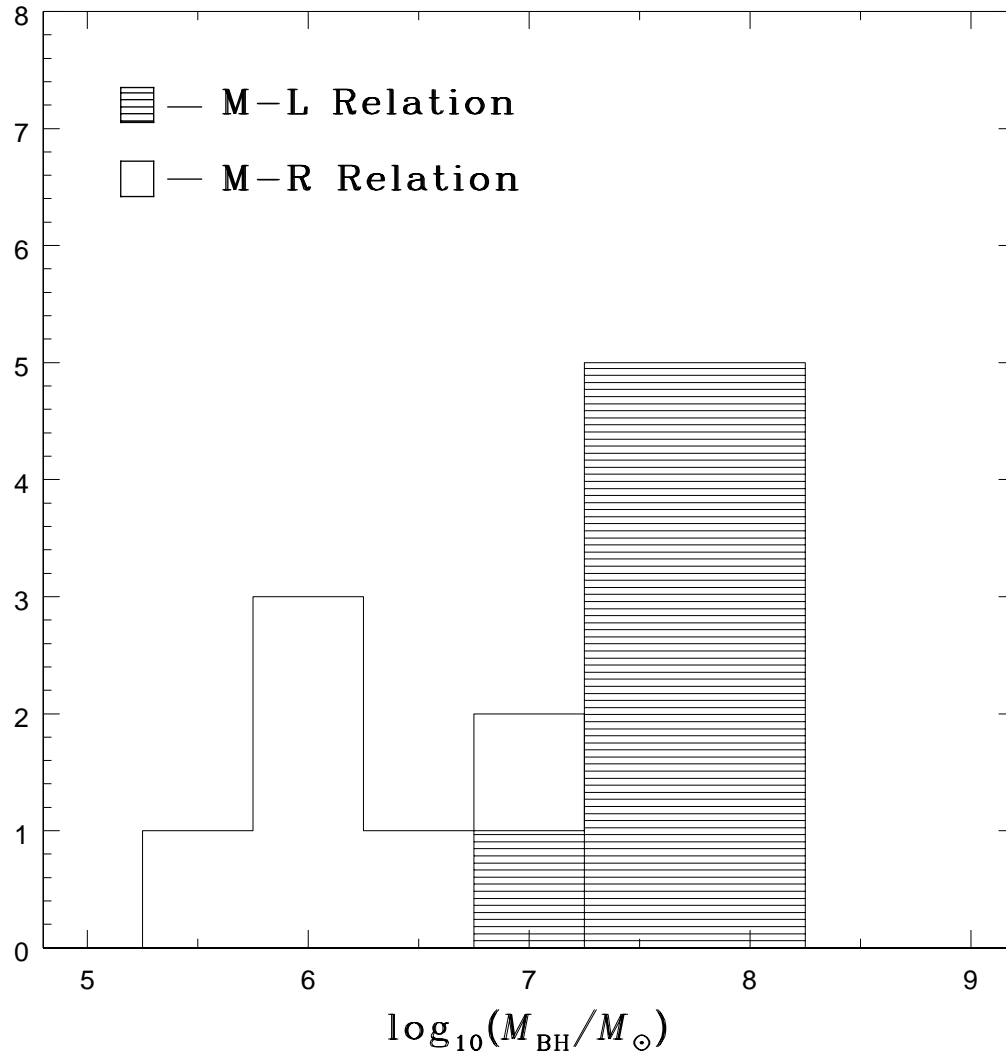


FIG. 15.— Histogram showing the distribution of black hole masses derived in this study.

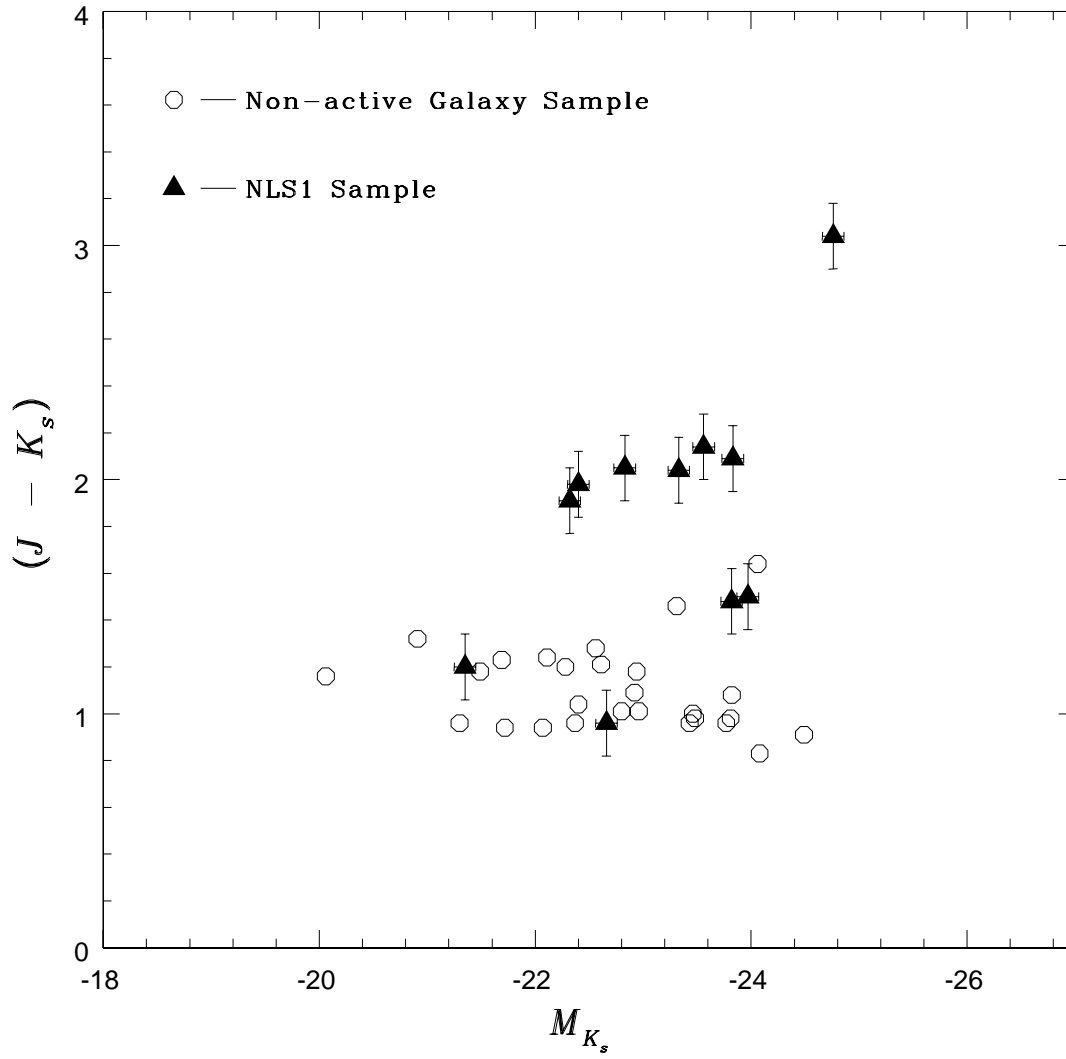


FIG. 16.— Comparison of the bulge $(J-K_s)$ colors for a sample of non-active galaxies and NLS1s. Open circles denote the non-active galaxy sample. NLS1 galaxies are denoted by filled triangles.